Top Organomet Chem
https://doi.org/10.1007/3418_2020_48

Characterizing the Metal–Ligand Bond Strength via Vibrational Spectroscopy: The Metal–Ligand Electronic Parameter (MLEP)

Elfi Kraka and Marek Freindorf

Contents

Abstract The field of organometallic chemistry has tremendously grown over the past decades and become an integral part of many areas of chemistry and beyond. Organometallic compounds find a wide use in synthesis, where organometallic compounds are utilized as homogeneous/heterogeneous catalysts or as stoichiometric reagents. In particular, modifying and fine-tuning organometallic catalysts has been at the focus. This requires an in-depth understanding of the complex metal–

In memoriam of Dieter Cremer.

E. Kraka (✉) and M. Freindorf
Computational and Theoretical Chemistry Group (CATCO), Department of Chemistry, Southern Methodist University, Dallas, TX, USA
e-mail: ekraka@smu.edu

ligand (ML) interactions which are playing a key role in determining the diverse properties and rich chemistry of organometallic compounds. We introduce in this article the metal–ligand electronic parameter (MLEP), which is based on the local vibrational ML stretching force constant, fully reflecting the intrinsic strength of this bond. We discuss how local vibrational stretching force constants and other local vibrational properties can be derived from the normal vibrational modes, which are generally delocalized because of mode–mode coupling, via a conversion into local vibrational modes, first introduced by Konkoli and Cremer. The MLEP is ideally suited to set up a scale of bond strength orders, which identifies ML bonds with promising catalytic or other activities. The MLEP fully replaces the Tolman electronic parameter (TEP), an indirect measure, which is based on the normal vibrational CO stretching frequencies of $[R_nM(CO)_mL]$ complexes and which has been used so far in hundreds of investigations. We show that the TEP is at best a qualitative parameter that may fail. Of course, when it was introduced by Tolman in the 1960s, one could not measure the low-frequency ML vibration directly, and our local mode concept did not exist. However, with these two problems solved, a new area of directly characterizing the ML bond has begun, which will open new avenues for enriching organometallic chemistry and beyond.

Keywords Local vibrational mode · Tolman electronic parameter · Transition metals · Vibrational spectroscopy

Abbreviations

ACS	Adiabatic connection scheme
BDE	Bond dissociation energy
BSO	Bond strength order
CEP	Computational electronic parameter
DFT	Density functional theory
LEP	Lever electronic parameter
LTEP	Local Tolman electronic parameter
MC	Metal carbon
MD	Molecular dynamics
ML	Metal ligand
MLEP	Metal–ligand electronic parameter
NHC	N-heterocyclic carbene
[NiFe]	Nickel iron hydrogenase
PES	Potential energy surface
QALE	Quantitative analysis of ligand effects
TEP	Tolman electronic parameter
ZPE	Zero-point energy

1 Introduction

Since French chemist Louis Claude Cadet de Gassicourt synthesized the first organometallic compound tetramethyldiarsine in 1706 [1], organometallic chemistry has tremendously grown and become an integral part of many areas of chemistry and beyond [2–12]. A number of researchers have been awarded the Nobel Prize in Chemistry for their work in the area of organometallic chemistry:

1912 – Victor Grignard, discovery of the Grignard Reagent, and Paul Sabatier, hydrogenation of organic species in the presence of metals
1963 – Karl Ziegler and Giulio Natta, Ziegler–Natta catalyst
1973 – Geoffrey Wilkinson and Ernst Otto Fischer, sandwich compounds
2001 – William Standish Knowles, Ryoji Noyori, and Karl Barry Sharpless, asymmetric hydrogenation
2005 – Yves Chauvin, Robert Grubbs, and Richard Schrock, metal-catalyzed alkene metathesis
2010 – Richard F. Heck, Ei-ichi Negishi, and Akira Suzuki, palladium-catalyzed cross-coupling reactions [13]

Organometallics are strictly defined as chemical compounds, which contain at least one bonding interaction between a metal and a carbon atom belonging to an organic molecule. However, aside from bonds to organyl fragments or molecules, bonds to "inorganic" carbon, like carbon monoxide (metal carbonyls), cyanide, or carbide, are generally considered as organometallic compounds as well. Likewise, in addition to the traditional main group metals [4–16] and transition metals [2], lanthanides and actinides [17, 18], as well as semimetals, i.e., elements such as boron, silicon, arsenic, and selenium [19, 20], are also considered to form organometallic compounds, e.g., organoboranes [21], broadening the range of organometallic compounds substantially.

One of the major advantages of organometallic compounds is their high reactivity, which finds wide use in synthesis, where organometallic compounds are utilized as homogeneous/heterogeneous catalysts or as stoichiometric reagents [22–28]. Major industrial processes using organometallic catalysts include hydrogenation, hydrosilylation, hydrocyanation, olefin metathesis, alkene polymerization, alkene oligomerization, hydrocarboxylation, methanol carbonylation, and hydroformylation, to name just a few [9, 29–31]. Organometallic complexes are also frequently used in cross-coupling reactions [32, 33], and they have attracted a lot of attention in the field of organometallic-mediated radical polymerization [34–38]. The production of fine chemicals relies on soluble organometallic complexes or involves organometallic intermediates, which often guarantee stereospecific products [7]. A recently evolving field is organometallic electrochemistry, which is devoted to finding solutions for the production of reliable, affordable, and environmentally friendly energy, fuels, and chemicals such as methanol or ammonia [39, 40]. Organometallic compounds have recently been discussed as an excellent alternative to the organic active layers used for solar cells or other light-emitting devices, due to their better properties such as thermal and chemical stability [41], and

it has been suggested that organometallic benzene derivatives may even serve as potential superconducting materials [42].

Organometallic catalysis has allowed the development of an impressive number of chemical transformations that could not be achieved using classical methodologies. Most of these reactions have been accomplished in organic solvents, and in many cases in the absence of water, and under air-free conditions. The increasing pressure to develop more sustainable transformations has stimulated the discovery of metal-catalyzed reactions that can take place in water. A particularly attractive extension of this chemistry consists of the use of biologically relevant aqueous solvents, as this might set the basis to transform catalytic metal complexes into biological settings [8, 11, 43–45]. These trends go in line with the recently invoked interest of pharmaceutical research and development for organometallics [46], in particular their use as potential anticancer drugs [47–49].

There is a continuous scientific endeavor being aimed at optimizing currently applied organometallic compounds and/or finding new ones with advanced properties and a broader scope of applications. In particular, modifying and fine-tuning homogeneous organometallic catalysts has been at the focus. However, there is a huge number of possible combinations between one of the 28 transition metals of the first, second, and third transition metal period (excluding Tc) or one of the 12 metals of periods 2–6 and an even larger amount of possible ligands (L). Attempts to find suitable organometallic complexes for catalysis reach from trial-and-error procedures to educated guesses and model-based strategies [50–58], which is nowadays strongly supported and guided by quantum chemical catalyst design exploring the catalytic reaction mechanism [59] or the physical properties of the catalyst [60]. Physical property-based approaches, which recently started to involve data science and machine learning techniques, provide the ability to examine large swaths of chemical space [61, 62], but the translation of this information into practical catalyst design may not be straightforward, in particular if the proposed properties do not directly relate to measurable quantities.

In this connection, one has searched since decades for measurable parameters that can be used as suitable descriptors to assess the catalytic activity of a metal complex, mainly focusing on identifying possible metal–ligand (ML) bond descriptors. The ML interaction, often highly covalent in nature in the case of organometallics, plays a key role in determining their diverse properties and rich chemistry, combining aspects of traditional inorganic and organic chemistry. Therefore, the detailed understanding of the ML bond is a necessary prerequisite for the fine-tuning of existing and the design of the next generation of organometallic catalysts. Two popular strategies to describe the catalytic activity of a transition metal complex in homogeneous catalysis as a function of the ML bond are based (1) on the ML bond dissociation energies (BDEs) [63–68] and (2) on molecular geometries to predict via BDE values and/or bond lengths the ease replacement of a given ligand or the possibility of enlarging the coordination sphere of a transition metal during catalysis. While these attempts have certainly contributed to the chemical understanding of metal and transition metal complexes, one has to realize that BDE values or bond lengths provide little insight into the intrinsic strength of the ML bond. The BDE is a reaction parameter that includes all changes, which take place during the dissociation

process. Accordingly, it includes any (de)stabilization effects of the products to be formed. The magnitude of the BDE reflects the energy needed for bond breaking but also contains energy contributions due to geometry relaxation and electron density reorganization in the dissociation fragments. Therefore, the BDE is not a suitable measure of the intrinsic strength of a chemical bond as it is strongly affected in non-predictable ways by the changes of the dissociation fragments. Accordingly, its use has led in many cases to a misjudgment of bond strength [69–74]. Also the ML bond length is not a qualified bond strength descriptor. Numerous cases have been reported illustrating that a shorter bond is not always a stronger bond [75–79]. Other computational approaches utilized to determine the strength of the ML bond include molecular orbital approaches [80, 81] or energy decomposition methods [82–84]. However, also these approaches provide more qualitative rather than quantitative results [69, 85]. On the other hand, detailed information on the electronic structure of a molecule and its chemical bonds is encoded in the molecular normal vibrational modes [86]. Therefore, vibrational spectroscopy should provide a better basis for a quantitative bond strength descriptor, which will be discussed in the next section.

2 The Tolman Electronic Parameter (TEP)

Experimentalists have used vibrational properties to describe chemical bonding including metal and transition metal catalysts for a long time [87–113] despite the fact that the rationalization of this use was never derived on a physically or chemically sound basis. Vibrational force constants seemed to be the best choice for describing the strength of chemical bonds, because they are independent of the atomic masses. However, it turned out that force constants derived from normal vibrational modes are dependent on the coordinates used to describe the molecule [114–118]. Therefore, the use of normal vibrational frequencies, which are directly available from experiment, was suggested. Because of the relatively large mass of M, ML vibrational frequencies appear in the far-infrared region, which was experimentally not accessible in the early 1960s. Therefore, the idea of a spectator ligand came up, which should have a high stretching frequency, i.e., easy to measure, and which was well-separated from all other frequencies in the spectrum. The metal spectator stretching frequency had to be sensitive to the strength of the ML bond and any electronic changes at M resulting from modifications of L, and it had to be common to most transition metal complexes. This idea was realized in several investigations on transition metal complexes, whereas suitable spectator and sensor ligands such as nitriles, isonitriles, and nitrosyl and carbonyl groups were tested, assuming that the CN, NC, NO^+, or CO stretching frequencies are sensitive with regard to the electronic configuration of M in the transition metal complex and a given ML bond, so that a spectroscopical (*indirect*) description of the latter seemed to be possible. Strohmeier's work on chromium, vanadium, manganese, tungsten, and other complexes [119, 120] made the lead in the field of metal–ligand

investigations with contributions from Fischer [121], Horrocks [122, 123], and Cotton [124–127]. Strohmeier ordered transition metals according to their π-donor ability: Cr > W > Mo > Mn > Fe. The overall proof of concept which emerged from these more or less scattered studies was that L acts as a σ-donor and/or a π-acceptor according to which the electron density at M is changed. This change can be monitored by the metal spectator ligand stretching frequency, which provides indirect evidence on the nature of L and the ML bond. However, it was the pioneering work of Tolman who combined and systemized these findings, culminating in the Tolman electronic parameter (TEP) as ML bond strength measure [128–130]. Originally, Tolman focused on tertiary phosphines (L = PR_3) interacting with a nickel–tricarbonyl rest, where the three CO ligands take the role of a spectator group measuring the interaction of L with Ni. Tolman defined the TEP as the A_1-symmetrical CO stretching frequency of the nickel–tricarbonyl–phosphine complex according to the following relationship:

$$\mathrm{TEP} = \omega(\mathrm{Ni;CO},A_1) = 2,056 + p_L \tag{1}$$

with P(t-Bu)$_3$ as a suitable reference with $p_L = 0$ and ω(CO, A_1) = 2,056 cm^{-1}. Tolman considered P(t-Bu)$_3$ as the most basic phosphine because of its strong σ-donor and absent π-acceptor ability. This leads to an increase of the electron density at Ni, which is transferred via the *d*-orbitals into the antibonding $\pi^\star$(CO) orbitals as sketched in Fig. 1a, b.

The CO bond length is increased, and the A_1-symmetrical CO stretching mode is redshifted to the value of 2,056 cm^{-1} compared to the CO stretching frequency in carbon monoxide of 2,071 cm^{-1} [132]. Any other, less basic phosphine leads to a lower electron density at Ni and thereby to a higher CO stretching frequency ω(L) and the ligand-specific increment $p_L = \omega(\mathrm{L}) - 2,056$. In this way, the basicity of phosphine ligands can be estimated by simply measuring the vibrational spectra (infrared or Raman) of the corresponding nickel–tricarbonyl–phosphine complex. Tolman used phosphine ligands because they cover a wide range of distinct electronic and steric properties, seldom participate directly in the reactions of a transition metal complex, and can they be used to modulate the electronic properties of the adjacent metal center. In addition, he relied on the following important assumptions:

1. ω(CO, A_1) is well separated from other frequencies, so it can be easily measured and identified in the IR spectrum.
2. The ω(CO, A_1) stretching mode does not couple with other vibrational modes, i.e., can be considered as *local* mode.
3. There is a general correlation between ω(CO, A_1) and ω(ML).

In literally hundreds of studies on transition metal–carbonyl complexes, the original Tolman concept has been applied, and in some studies, its general applicability has been tested. For example, Otto and Roodt [133] fitted the CO frequencies measured by Strohmeier for *trans*-[Rh(CO)ClL_2] (Rh-Vaska) complexes with the CO frequencies of Tolman's nickel–tricarbonyl–phosphines and obtained a quadratic relationship, which suggests that besides the σ-donor activity of the trialkyl

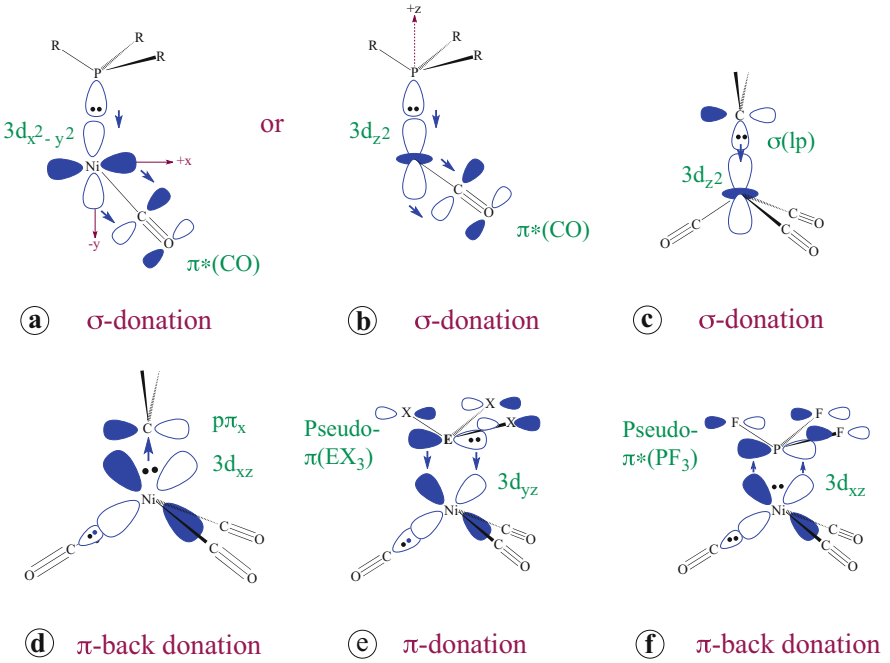

Fig. 1 Schematic overview over possible orbital interactions between ligand L and the $[Ni(CO)_3]$ group in $[Ni(CO)_3\ L]$ complexes. Reproduced from Ref. [131] with permission of the Royal Society of Chemistry

phosphines, for other ligands, a second ML bonding mechanism in a form of a strong π-acceptor ability becomes dominant. A series of 14 linear relationships between the TEP and the CO stretching frequencies of V, Cr, Mo, W, Mn, Fe, and Rh complexes has been published by Kühl [134]:

$$\mathrm{TEP} = A\omega(\mathrm{M;CO},A_1) + B \tag{2}$$

where each new type of a given transition metal complex (with the same transition metal (M)) required a different relationship with correlation coefficients R^2 ranging from 0.799 to 0.996. A significant data scattering suggested that for a given transition metal (M), complexes of the type $[R_nM(CO)_mL]$ may be subject to different ML bonding mechanisms depending on the ligands R and L and the coordination numbers m and n. ML bonding might also be affected by the environment (solvent, crystal state, etc.). As indicated in Fig. 1c–d, there may be also $[R_nM(CO)_mL]$ interactions which are not reflected by $\omega(\mathrm{CO}, A_1)$. In addition, Tolman's choice of the t-Bu reference has been challenged by Arduengo's N-heterocyclic carbenes (NHCs) [135–137], which are stronger σ-donors than the t-Bu reference, so that a TEP $< 2{,}056\ \mathrm{cm}^{-1}$ and a negative p_L value results.

Parallel to the experimental efforts obtaining TEP values, computational chemists started to determine CO stretching frequencies of carbonyl–metal complexes in the

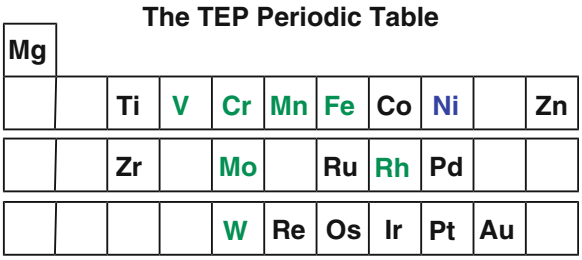

Fig. 2 Use of the TEP throughout the periodic table. Experimentally derived TEPs have been discussed for Ni (blue) [128–130, 138, 151–160] which were correlated with the TEPs of transition metals given in green by Kühl [134]. Reproduced from Ref. [131] with permission of the Royal Society of Chemistry. For specific references, see Pd [161–168], Pt [164, 169], Co [170, 171], Rh [153, 166, 172–175], Ir [153, 163, 175–180], Fe [172, 181], Ru [182–188], Os [189, 190], Re [191–193], Mn [119, 120, 194], Cr [122, 195–198], Mo [155, 173, 195], W [170, 199], V [120], Ti [200, 201], Zr [202], Mg [120], Cu [203, 204], Au [168, 205–208], and Zn [162]

harmonic approximation for molecules in the gas phase and to use them as a computational electronic parameter (CEP) for the description of ML bonding [138]. Most of the computational investigations suggested that CEPs obtained for Ni, Ir, or Ru complexes correlate well with the experimental TEPs [139–144], provided model chemistries are applied, which are suitable for the description of metal complexes [139, 141, 145]. CEP values based on semiempirical calculations were published for $LMo(CO)_5$, $LW(CO)_5$, and CpRh(CO)L complexes [146] or rhodium Vaska-type complexes [147]. However, the results depend on the parametrization of the used semiempirical method. In addition to gas phase TEPs, CEPs were also calculated for CO adsorbed by Ni–Au clusters [148]. Several review articles have summarized the experimental and theoretical work in this field [134, 149, 150]. Figure 2 gives on overview of the use of the TEP in a form of a *TEP periodic table*, where the manifold of transition metal complexes for a given M can be retrieved from the literature given in the figure caption.

As a consequence of the widespread use of the TEP, attempts to relate or complement it by other measured or calculated properties of the transition metal complex emerged over time. Tolman himself realized that the bulkiness of a ligand can outweigh the electronic factors, which was the reason why he introduced the cone angle θ as a measure for the steric requirements of the ligand [128, 130]. The Lever electronic parameter (LEP) was introduced, which is based on the ratio of the redox potentials of closely related complexes such as those of Ru(III) and Ru(II), which can be electrochemically determined [209, 210], and which can be set into a relationship to the TEP [138]. It has been disputed whether the molecular electrostatic potential can be used to derive the CO stretching frequencies of transition metal–carbonyl complexes [211, 212]. Alyea and co-workers [213] suggested ways of differentiating between σ and π effects influencing the CO stretching frequencies by referring to thermochemical data such as pK_a values. Giering combined electronic and steric effects to what he coined the *quantitative analysis of ligand effects (QALE)* model [212]. Coll and co-workers introduced an average local ionization energy I(**r**)

that, if integrated over the van der Waals surface of ligand L, can be related to the TEP and Tolman's cone angle, as was demonstrated for phosphines and phosphites. However, this approach turned out to be only reliable for ligands (L) with high polarizability [214].

Although the TEP is still today one of the most popular measures used by the experimental and computational chemistry community for quantifying the catalytic activity of transition metal complexes based on vibrational spectroscopy, criticism on the TEP has been raised by several authors in the recent literature [139, 177, 192, 205, 206, 215–221], in particular with regard to the validity of Tolman's original assumption of uncoupled CO stretching modes. The normal vibrational modes in a molecule always couple [86]. There are only a few examples for uncoupled, non-delocalized, i.e., *local*, vibrational modes. The bending vibration of the water molecule is such an example of a local vibration, where the frequency is not contaminated by coupling contributions. In general, mode–mode coupling depends on the orientation of the mode vectors: vibrational modes with orthogonal mode vectors do not couple. Also, difference in the atomic masses can suppress coupling. For example, for the light–heavy–light arrangement of an acyclic three-atom molecule, the central atom can function as a "wall," thus largely suppressing mode–mode coupling [222].

The TEP is based on measured or calculated normal mode CO stretching frequencies, which may be effected by mode–mode coupling between the CO stretchings or even between the CO and the MC stretching modes. There are two different coupling mechanisms between vibrational modes as a consequence of the fact that there is a kinetic and a potential contribution to the energy of a vibrational mode [86]. The electronic coupling between modes is reflected by the off-diagonal elements of the force constant matrix. By diagonalizing the force constant matrix $\mathbf{F}^q$ expressed in terms of internal coordinates q_n, i.e., a transformation to normal coordinates and related normal modes, the electronic mode–mode coupling is eliminated. However, the resulting normal mode force constants are still contaminated by kinematic mode–mode coupling, and as described above, they depend on the internal coordinates chosen to describe the molecular geometry. Already in the 1960s, Decius [117] attempted to solve the force constant problem by using the inverse force constant matrix $\Gamma = (\mathbf{F}^q)^{-1}$ and introducing the so-called compliance constants Γ_{nn} as bond strength descriptors. However, the relationship of the compliance constants to normal or other vibrational modes was unclear. Hence, the compliance constants remained force constants without a mode and a frequency. Also a given Γ_{nn} is related to off-diagonal elements Γ_{mn} ($m \neq n$), the physical meaning of which is unclear. This led to criticism and questions about the usefulness of compliance constants [223]. For example, why should one only use the diagonal Γ_{nn} terms without considering the role of the off-diagonal Γ_{mn} terms when chemical bonds were described. There were also questions about the physical meaning of compliance constants related to redundant internal coordinates. Therefore, needed for an advanced TEP model are local vibrational modes, which fulfill the following requirements:

1. They must be uniquely related to both experimentally derived and calculated normal modes.
2. Each local mode must be independent of the isotope composition of the rest of the molecule.
3. Each local mode must possess a corresponding local mode force constant, frequency, mass, and intensity.
4. The local mode force constant must be independent of the internal coordinates used for the description of the molecular geometry.

3 Local Vibrational Mode Analysis

As will be shown in this section, the Konkoli–Cremer local vibrational modes fulfill all of these requirements. In 1998, Konkoli and Cremer [78, 224, 225] derived for the first time local vibrational modes directly from normal vibrational modes by solving the mass-decoupled Euler–Lagrange equations, i.e., by solving the local equivalent of the Wilson equation for vibrational spectroscopy [86]. They developed the *leading parameter principle* [224], which states that for any internal, symmetry, curvilinear, etc. coordinate, a local mode can be defined. This mode is independent of all other internal coordinates used to describe the geometry of a molecule, which means that it is also independent of using redundant or nonredundant coordinate sets. The number of local vibrational modes can be larger than N_{vib} (N: number of atoms, $N_{\text{vib}} = 3N - 6$ for a nonlinear and $3N - 5$ for a linear molecule), and therefore, it is important to determine these local modes, which are essential for the reproduction of the normal modes. This can be accomplished via an adiabatic connection scheme (ACS), which relates local vibrational frequencies to normal vibrational frequencies by increasing a scaling factor λ from zero (local frequencies) to 1(normal frequencies). For a set of redundant internal coordinates and their associated local modes, all those local mode frequencies converge to zero for $\lambda \rightarrow 1$, which do not contribute to the normal modes, so that a set of meaningful N_{vib} local modes remains [85, 226]. In this way, a 1:1 relationship between local (adiabatically relaxed) vibrational modes and normal vibrational modes has been established [85].

Cremer and co-workers developed a method for calculating from a complete set of N_{vib} measured fundamental frequencies, the corresponding local mode frequencies [76]. In this way, one can distinguish between calculated harmonic local mode frequencies (force constants) and experimentally based local mode frequencies (force constants), which differ by anharmonicity effects [227, 228]. Zou and co-workers [85] proved that the reciprocal of the compliance constant of Decius is identical with the local force constant of Konkoli and Cremer, so that for the first time the physical meaning of the compliance constants could be established. They could also show that the local vibrational modes of Konkoli and Cremer are the only modes, which uniquely relate to the normal vibrational modes [85]. A local stretching force constant associated with the bond length q_n is related to the second derivative of the molecular energy with regard to q_n, i.e., to the curvature of the

Born–Oppenheimer potential energy surface (PES) in the direction of the internal coordinate q_n. For an increasing bond length described by q_n, this coordinate becomes the coordinate of bond dissociation. Zou and Cremer [229] demonstrated that by approximating the PES in this direction by a Morse potential and freezing the electron density during the dissociation process, the local stretching force constant is directly related to the intrinsic strength of a bond, which qualifies the local stretching force as unique quantitative bond strength measure.

Before proceeding with the derivation of the local vibrational modes, it is useful to point out that the term *local mode* has been used by different authors in different ways:

1. The Konkoli–Cremer local vibrational modes are the unique and only equivalents of the normal modes, which are obtained by utilizing the Wilson equation of vibrational spectroscopy [86]. The Konkoli–Cremer local modes are related to the *isolated* modes of McKean obtained by isotope substitution [230], which represent a good approximation for the Konkoli–Cremer local vibrational modes.
2. Henry and co-workers [231–235] use the term local modes in connection with local mode (an)harmonic oscillator models to describe the overtones of XH stretching modes. Therefore, microwave spectroscopists and other experimentalists refer to *local modes* often in connection with overtone spectroscopy.
3. Reiher and co-workers [236–238] calculate unitarily transformed normal modes of a polymer being associated with a given band in the vibrational spectrum, where the criteria for the transformation are inspired by those applied for the localization of molecular orbitals. The authors speak in this case of local vibrational modes, because the modes are localized in just a few units of a polymer. However, these so-called localized modes are still delocalized within the polymer units.
4. In solid-state physics, the vibrational mode(s) of an impurity in a solid material is (are) called local modes [239, 240].

3.1 Theory of Local Vibrational Modes

In Eq. (3), the Wilson equation of vibrational spectroscopy is given [86, 231, 241, 242]:

$$\mathbf{F}^x\widetilde{\mathbf{L}} = \mathbf{M}\widetilde{\mathbf{L}}\Lambda \tag{3}$$

where $\mathbf{F}^x$ is the force constant matrix expressed in Cartesian coordinates x_i ($i = 1, \cdots 3N$); $\mathbf{M}$ is the mass matrix, matrix $\widetilde{\mathbf{L}}$ collecting the vibrational eigenvectors $\mathbf{l}_\mu$ in its columns; and Λ is a diagonal matrix with the eigenvalues λ_μ, which leads to the (harmonic) vibrational frequencies ω_μ according to $\lambda_\mu = 4\pi^2c^2\omega_\mu^2$. The number of vibrational modes is given by N_{vib}, i.e., translational and rotational motions of the molecule are already eliminated. The tilde above a vector or matrix symbol indicates

mass weighting. By diagonalizing the force constant matrix according to $\widetilde{\mathbf{L}}^{\dagger}\mathbf{F}^{x}\widetilde{\mathbf{L}} = \Lambda$, the normal mode eigenvectors and eigenvalues are obtained.

Usually, the normal mode vectors $\widetilde{\mathbf{l}}_{\mu}$ are renormalized according to $\mathbf{L} = \widetilde{\mathbf{L}}\left(\mathbf{M}^{R}\right)^{1/2}$, where the elements of the mass matrix $\mathbf{M}^{R}$ are given by $m_{\mu}^{R} = \left(\widetilde{\mathbf{l}}_{\mu}^{\dagger}\widetilde{\mathbf{l}}_{\mu}\right)^{-1}$ and represent the reduced mass of mode μ. Equation 3 can be written in different ways. For example, without mass weighting as shown in Eq. (4):

$$\mathbf{F}^{x}\mathbf{L} = \mathbf{M}\mathbf{L}\Lambda \tag{4}$$

One obtains $\mathbf{L}^{\dagger}\mathbf{F}^{x}\mathbf{L} = \mathbf{K}$ and $\mathbf{L}^{\dagger}\mathbf{M}\mathbf{L} = \mathbf{M}^{R}$, which define the diagonal normal force constant matrix $\mathbf{K}$ and the reduced mass matrix $\mathbf{M}^{R}$, respectively.

One can express the molecular geometry in terms of internal coordinates q_n rather than Cartesian coordinates x_n, and by this, the Wilson equation adopts a new form: [86]

$$\mathbf{F}^{q}\widetilde{\mathbf{D}} = \mathbf{G}^{-1}\widetilde{\mathbf{D}}\Lambda \tag{5}$$

where $\widetilde{\mathbf{D}}$ collects the normal mode vectors $\widetilde{\mathbf{d}}_{\mu}$ ($\mu = 1, \ldots, N_{\text{vib}}$) column-wise, and matrix $\mathbf{G} = \mathbf{B}\mathbf{M}^{-1}\mathbf{B}^{\dagger}$ (Wilson **G**-matrix) gives the kinetic energy in terms of internal coordinates [86]. The eigenvector matrix $\widetilde{\mathbf{D}}$ has the property to diagonalize $\mathbf{F}^{q}$ and to give $\widetilde{\mathbf{D}}^{\dagger}\mathbf{F}^{q}\widetilde{\mathbf{D}} = \Lambda$. If one does not mass weight the matrix $\mathbf{D}$ and works with $\mathbf{F}^{q}\mathbf{D} = \mathbf{G}^{-1}\mathbf{D}\Lambda$, diagonalization leads to $\mathbf{D}^{\dagger}\mathbf{F}^{q}\mathbf{D} = \mathbf{K}$.

Properties of a Local Mode The local mode vector $\mathbf{a}_n$ associated with the internal coordinate q_n, which *leads* the *n*th local mode, is given by [224]:

$$\mathbf{a}_n = \frac{\mathbf{K}^{-1}\mathbf{d}_n^{\dagger}}{\mathbf{d}_n\mathbf{K}^{-1}\mathbf{d}_n^{\dagger}} \tag{6}$$

where the local mode is expressed in terms of normal coordinates Q_{μ}. $\mathbf{K}$ is the diagonal normal mode force constant matrix (see above) and $\mathbf{d}_n$ is a row vector of the matrix $\mathbf{D}$. The local mode force constant k_n^a of mode n (superscript a denotes an adiabatically relaxed, i.e., local mode) is obtained via Eq. (7):

$$k_n^a = \mathbf{a}_n^{\dagger}\mathbf{K}\mathbf{a}_n = \left(\mathbf{d}_n\mathbf{K}^{-1}\mathbf{d}_n^{\dagger}\right)^{-1} \tag{7}$$

Local mode force constants, contrary to normal mode force constants, have the advantage of being independent of the choice of the coordinates used to describe the molecule in question [76, 224]. In recent work, Zou and co-workers proved that the compliance constants Γ_{nn} of Decius [117] are simply the reciprocal of the local mode force constants: $k_n^a = 1/\Gamma_{nn}$ [85, 226, 243].

The reduced mass of the local mode $\mathbf{a}_n$ is given by the diagonal element G_{nn} of the **G**-matrix [224]. Local mode force constant and mass are needed to determine the local mode frequency ω_n^a

$$\left(\omega_n^a\right)^2 = 14\pi^2 c^2 k_n^a G_{nn} \tag{8}$$

Apart from these properties, it is straightforward to determine the local mode infrared intensity or the Raman intensity [244].

Adiabatic Connection Scheme (ACS) Relating Local to Normal Mode Frequencies With the help of the compliance matrix $\Gamma^q = (\mathbf{F}^q)^{-1}$, the vibrational eigenvalue (Eq. (5)) can be expressed as [85]:

$$(\Gamma^q)^{-1}\widetilde{\mathbf{D}} = \mathbf{G}^{-1}\widetilde{\mathbf{D}}\,\Lambda \tag{9}$$

$$\mathbf{G}\,\widetilde{\mathbf{R}} = \Gamma^q\widetilde{\mathbf{R}}\,\Lambda \tag{10}$$

where a new eigenvector matrix $\widetilde{\mathbf{R}}$ is given by:

$$\widetilde{\mathbf{R}} = (\Gamma^q)^{-1}\widetilde{\mathbf{D}} = \mathbf{F}^q\widetilde{\mathbf{D}} = \left(\widetilde{\mathbf{D}}^{-1}\right)^{\dagger}\mathbf{K} \tag{11}$$

Zou and co-workers partitioned the matrices Γ^q and **G** into diagonal (Γ_d^q and $\mathbf{G}_d$) and off-diagonal parts (Γ_{od}^q and $\mathbf{G}_{od}$) [85]:

$$\left(\mathbf{G}_d + \lambda\,\mathbf{G}_{od}\right)\widetilde{\mathbf{R}}_\lambda = \left(\Gamma_d^q + \lambda\,\Gamma_{od}^q\right)\widetilde{\mathbf{R}}_\lambda\Lambda_\lambda \tag{12}$$

The off-diagonal parts can be successively switched on by increasing a scaling factor λ from zero to one so that the local modes given by the diagonal parts ($\lambda = 0$) are adiabatically converted into normal modes defined by $\lambda = 1$. Each λ defines specific set of eigenvectors and eigenvalues collected in $\widetilde{\mathbf{R}}_\lambda$ and Λ_λ, respectively. Equation (12) is the basis for the ACS.

3.2 Application of the Local Vibrational Mode Analysis

The local mode analysis has been successfully applied to characterize covalent bonds [73, 75, 229, 245–248] and weak chemical interactions such as halogen [72, 249–252], chalcogen [253–255], pnicogen [256–258], and tetrel interactions [74] as well as H-bonding [227, 228, 259–263] and BH$\cdots\pi$ interactions [264, 265]. Recently, the local mode analysis was for the first time successfully applied to periodic systems [266, 267]. Some highlights include:

- The intrinsic bond strength of C_2 in its $^1\Sigma_g^+$ ground state could be determined by its local stretching force constant. In comparison with the local CC stretching force constants obtained for ethane, ethene, and acetylene, an intrinsic bond strength half way between that of a double bond and that of a triple bond was derived. These results, based on both measured and calculated frequency data, refute the verbose discussion of a CC quadruple bond [229].
- The modeling of liquid water with 50 mers and 1,000 mers using both quantum chemistry and molecular dynamics (MD) simulations at different temperatures led to a set of interesting results [260]. The local mode analysis revealed that there are 36 hydrogen bonds in water clusters of different strength. In warm water, the weaker H-bonds with predominantly electrostatic contributions are broken, and smaller water clusters with strong H-bonding arrangements remain that accelerate the nucleation process leading to the hexagonal lattice of solid ice. Therefore, warm water freezes faster than cold water in which the transformation from randomly arranged water clusters costs time and energy. This effect known in the literature as the *Mpemba effect*, according to its discovery by Mpemba in 1969 [268], could now for the first time be explained at the atomistic level.
- For the first time, nonclassical H-bonding involving a $BH\cdots\pi$ interaction was described utilizing both quantum chemical predictions and experimental realization. According to the Cremer–Kraka criterion for covalent bonding [269, 270], this interaction is electrostatic in nature and the local $BH\cdots\pi$ stretching force constant is as large as the H-bond stretching force constant in the water dimer [264, 265].
- A method for the quantitative assessment of aromaticity and antiaromaticity based on vibrational spectroscopy was developed [271], which led to a new understanding of the structure and stability of polycyclic gold clusters based on a new Clar's Aromaticity Rule equivalent [272, 273].

4 Assessment of the TEP with the Local Mode Analysis

The local mode analysis will be used in the following section to test Tolman's basic assumptions: (1) that the ω(CO, A_1) normal mode does not couple with other vibrational modes, and (2) that there is a general correlation between ω(CO, A_1) and ω(ML).

4.1 TEP and Mode–Mode Coupling

A potential contamination of the CO stretching frequencies due to mode–mode coupling was already considered by Crabtree and co-workers [138] who tried to correct computationally the CO stretching frequencies of 66 nickel–tricarbonyl

complexes [Ni(CO)$_3$L]. However, their attempt to eliminate mode–mode coupling by manipulating the Hessian of calculated second energy derivatives failed to remove the kinematic coupling between the CO stretching vibrations and other vibrations, as was pointed out by Kalescky and co-workers in their local mode study of Crabtree's 66 nickel–tricarbonyl complexes. This work led for the first time to decoupled, local CO stretching modes [145]. Setiawan and co-workers extended the original set of 66 nickel–tricarbonyl complexes to a more comprehensive set of 181 nickel–tricarbonyl complexes [Ni(CO)$_3$L], shown in Figs. 3 and 4, including besides phosphine ligands also nitrogen and cyano, amines, arsines, stilbines, bismuthines, boron compounds, carbonyl, thiocarbonyl, carbenes, water and ethers, thioethers, haptic ligands, and anions [274].

In Fig. 5a, the normal mode frequencies ω(CO, A_1) are correlated with the corresponding local mode frequencies ω^a(CO) for both experimental and calculated frequencies. If the TEP would be without any coupling errors, i.e., the normal mode ω(CO, A_1) stretching frequencies would be completely local as assumed by Tolman, all data points should be found along the dashed line, which defines mode-decoupled, i.e., local TEP values. Instead data points (experimental, brown color; calculated, green color, Fig. 5a) suggest more positive TEP values in particular with decreasing local CO stretching frequency. In other words, a lower CO stretching frequency does not necessarily indicate a stronger Ni–CO π-back bonding but a larger mode–mode coupling. It also seems that the ω(CO, A_1) stretching mode, chosen by Tolman, does not necessarily reflect the total red shift of the CO stretching as indicated in Fig. 1e–f. These findings hold for both measured and calculated TEP values (CEPs) excluding that the harmonic approximation used for the CEPs causes the deviation between normal and local mode frequencies.

The mode–mode coupling can also directly be assessed by the *coupling frequencies* ω_{coup}(CO) shown in Fig. 5b as function of ω^a(CO). They are defined as the difference between the local mode frequency and the corresponding normal mode frequency being connected via an ACS, i.e., $\omega_{\text{coup}} = \omega(\lambda = 1) - \omega(\lambda = 0)$, which reflects the changes in the local mode frequency $\omega^a = (\lambda = 0)$ caused by mode–mode coupling. Large coupling frequencies are obtained when the starting local mode frequencies are close or identical (degeneracy caused by symmetry) and the mass ratio of the vibrating atoms is comparable. The sum of local mode and coupling frequency is always identical to the corresponding normal mode frequency. When adding the sum of coupling frequencies to the sum of local mode frequencies, the zero-point energy (ZPE) is recovered [85]. Fig. 5b suggests qualitatively an inverse relationship between coupling frequencies and the local CO stretching frequencies, i.e., a smaller CO stretching frequency ω^a(CO) implies a larger mode–mode coupling. Anionic ligands with strong σ- and/or π-donor capacity lead to the largest errors as Ni–CO π-back bonding is connected with a change in the Ni–C bond and an increased Ni–C and CO coupling. This means that for neutral and anionic ligands, TEP errors of 40–100 cm^{-1} can be expected making the use of the uncorrected TEP highly questionable. Overall more electronegative ligands lead to higher TEP errors, whereas cationic ligands such as NO^+ or HC^+ give more reliable TEP values.

Detailed insight into mode–mode coupling can be obtained by two special features of the local mode analysis, which allow the comprehensive analysis of a

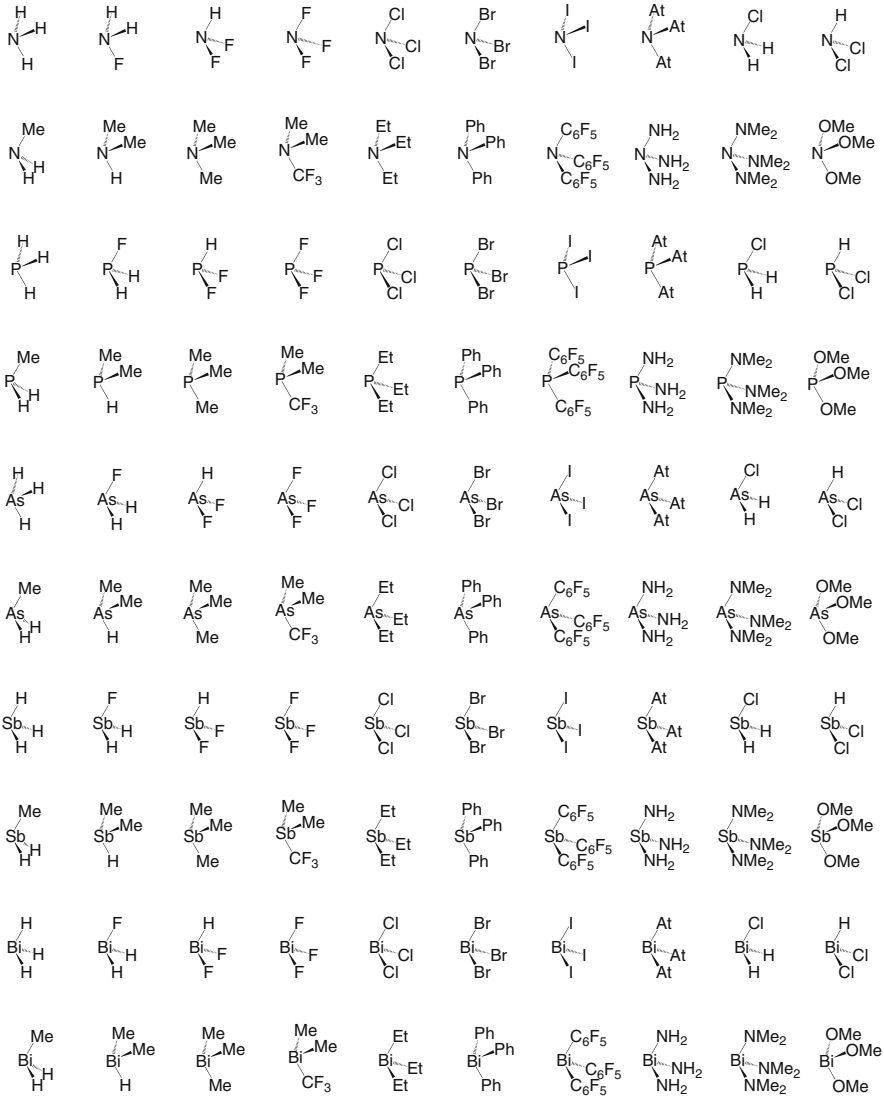

Fig. 3 Schematic representation of the 181 ligands of $[Ni(CO)_3L]$ complexes investigated by Setiawan and co-workers [274]: part 1. Reproduced from Ref. [274] with permission of the American Chemical Society

vibrational spectrum, (1) the adiabatic connection scheme (ACS) and (2) the decomposition of each normal mode into local mode contributions, which will be discussed in the following section for $[Ni(CO)_3F]^-$, the complex with the largest coupling error of 100 cm^{-1}. Figure 6a shows how the three equivalent local vibrational CO modes $\omega^a(5,6,7)$ of $[Ni(CO)_3F]^-$ are transformed into the A_1 normal mode ω_{18}, i.e., the TEP

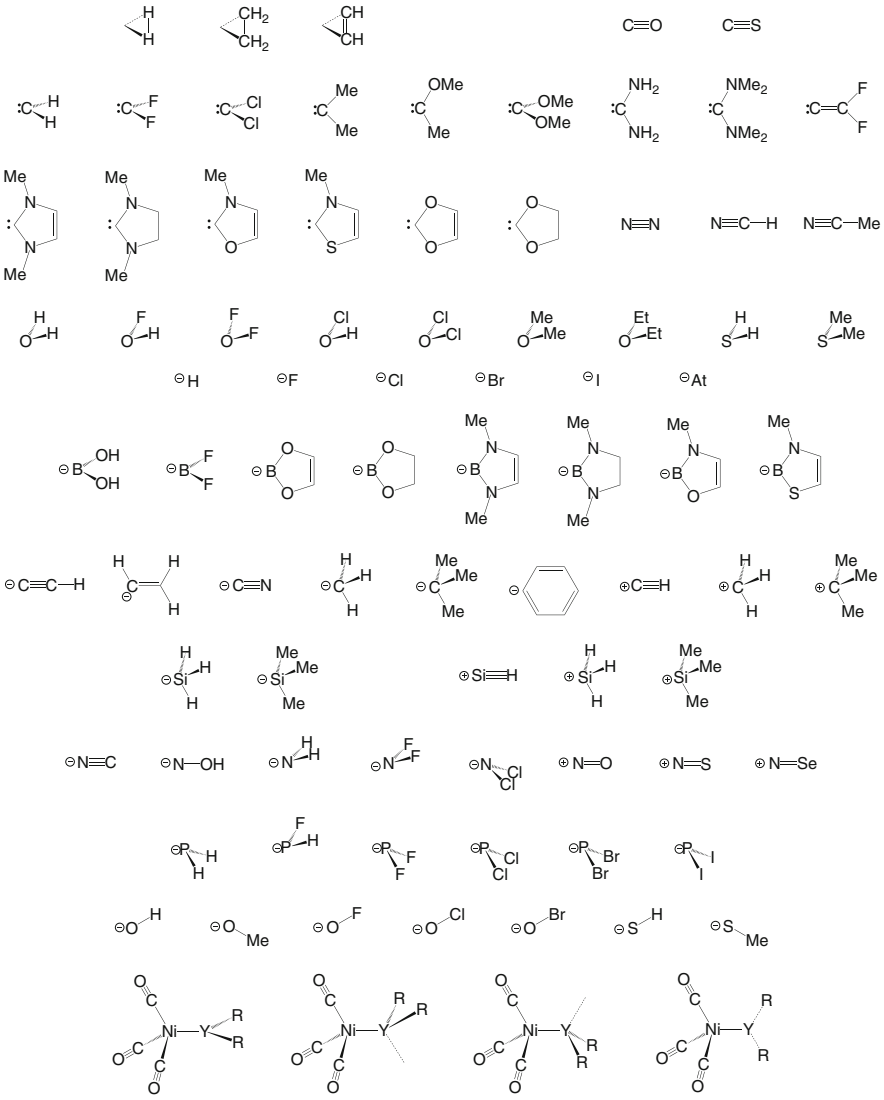

Fig. 4 Schematic representation of the 181 ligands of $[Ni(CO)_3L]$ complexes investigated by Setiawan and co-workers [274]: part 2. The four conformational possibilities of a complex are given in the bottom row. Reproduced from Ref. [274] with permission of the American Chemical Society

and into the two degenerate E normal modes ω_{16} and ω_{17} by switching on the masses via the perturbation parameter λ. The three equivalent local mode frequencies $\omega^a(5,6,7)$ ($\lambda = 0$) have a value of 2,019 cm^{-1} revealing a redshift of 225 cm^{-1} compared to the stretching frequency of carbon monoxide calculated at the same level of theory. Fully switching on the masses (endpoint: $\lambda = 1$) leads to a mass

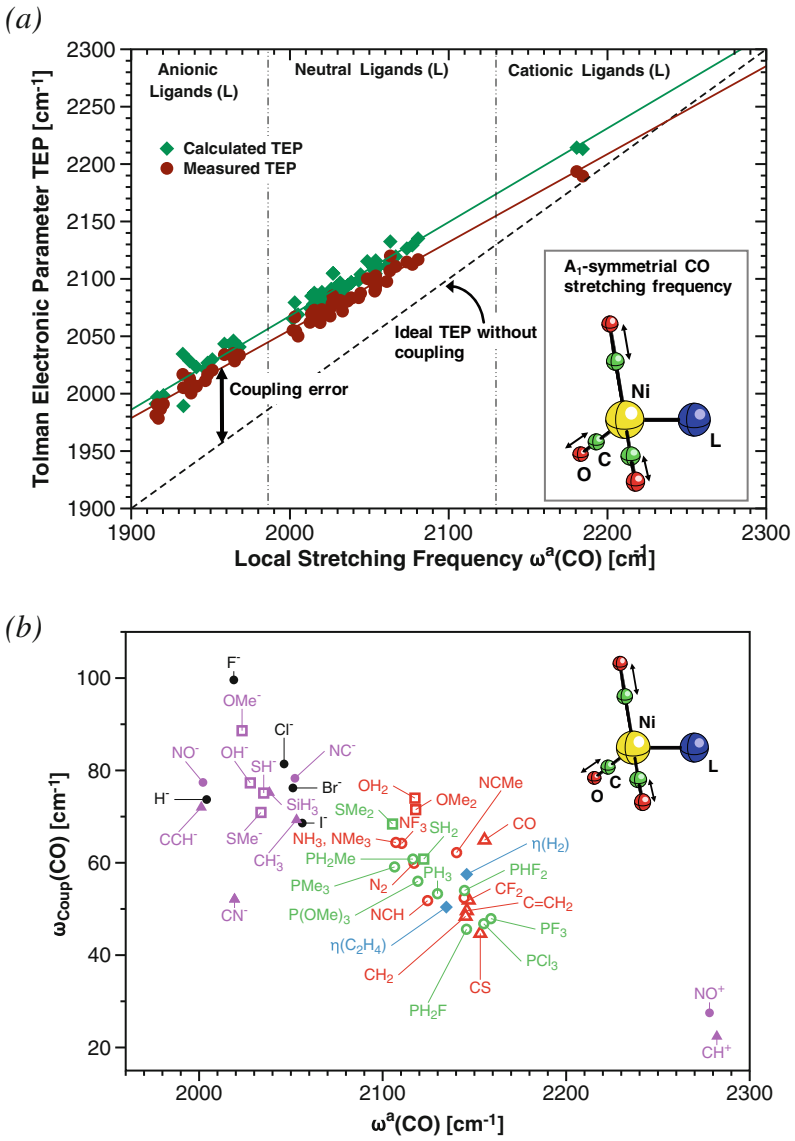

Fig. 5 Mode–mode coupling of the normal mode stretching frequencies ω(CO, A_1) corresponding to the TEP [131]. Calculated with the M06 functional [275] using Dunning's aug–cc–pVTZ basis set [276]. (**a**) Correlation between local mode stretching frequencies ω^a(CO) and normal mode stretching frequencies ω(CO, A_1) corresponding to the TEP for experimental and calculated harmonic vibrational frequencies. Reproduced from Ref. [131] with permission of the Royal Society of Chemistry. (**b**) Coupling frequencies ω_{coup}(CO) compared with the corresponding local mode stretching frequencies ω^a(CO). The TEP is stronger contaminated by ω_{coup}(CO) for weaker Ni–L bonds. Reproduced from Ref. [131] with permission of the Royal Society of Chemistry

splitting of 81 cm^{-1} resulting in the $\omega_{18}(A_1)$ frequency of 2,118 cm^{-1} and the two degenerate $\omega_{16,\ 17}(E)$ frequencies of 2,037 cm^{-1}. So the TEP is only redshifted by 116 cm^{-1} compared to carbon monoxide, in line with the finding that TEP values are generally higher in value than their local mode counterparts. The lowering of the local CO stretching frequency is the result of σ-donation and π-back donation involving both e_g and t_{2g} symmetrical 3d(Ni) orbitals (see Fig. 1). By using the normal A_1-symmetrical CO stretching frequency as a bond strength descriptor, the full amount of CO weakening cannot be correctly described, because of the mass-dependent splitting of A_1 and E-symmetrical modes. Figure 6a suggests that for $[Ni(CO)_3F]^-$, the degenerate $\omega_{16,17}(E)$ frequencies would have been a better choice as bond strength descriptors.

The ACS analysis can be complemented by a decomposition of the 18 normal modes of $[Ni(CO)_3F]^-$ into local mode contributions, as shown in Fig. 6b and Table 1. All CO stretching modes including the TEP couple to some extend with the NiC stretching modes, leading to a non-negligible admixture of about 4%. In summary, the local mode analysis is an essential tool for the quantification of mode–mode coupling, which depends on the nature of the ML bond, the symmetry of the complex, and its geometry. If for a given complex all N_{vib} normal vibrational frequencies are known (measured or computed), one can easily determine the local CO stretching frequencies and use these local, mode–mode coupling free frequencies, which we have coined LTEPs [274] instead of the TEPs as ML bond strength descriptors.

4.2 Correlation Between CO and ML Bonding

However, even if mode–mode coupling free LTEPs would be used, there is still an important open question, i.e., does the CO stretching frequency reflect ML bonding as assumed by Tolman? This question can be answered by comparing the local mode CO force constants k^a(CO) with the corresponding local NiL force constants k^a(NiL) (as shown in Fig. 7) for the set of 181 $[NiCO_3L]$ complexes [274]. Since (1) the local constants are independent of the choice of the coordinates used to describe the molecule under consideration and (2) they are directly linked to the intrinsic bond strength, we will use local mode force constants instead of local mode frequencies throughout the remainder of this work.

Clearly, there is no general relationship between k^a(CO) and k^a(NiL) for this large set of $[NiCO_3L]$ complexes calling Tolman's assumption into question. Subsets of data points belonging to a well-defined type of ligand show rather qualitative relationships, indicated by the different dashed blue lines in Fig. 7. This can be seen as an extension of Kühl's findings that for each transition metal complex with a different metal, i.e., V, Cr, Mo, W, Mn, Fe, or Rh, a different relationship has to be used [134]. The results presented in Fig. 7 show that even within the Ni–phosphine complexes, there is no unique relationship. One has to distinguish between normal trialkyl phosphines (purple filled dots in Fig. 7), phosphines with electronegative

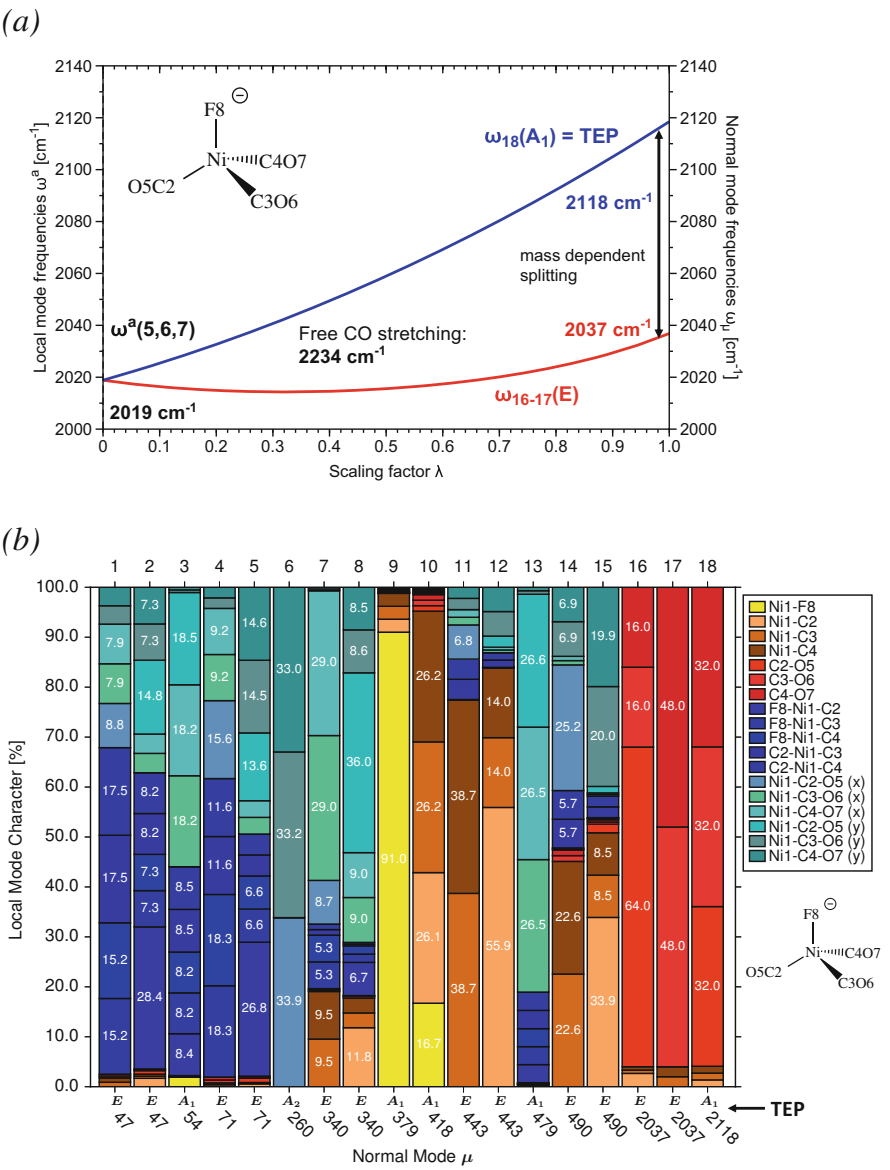

Fig. 6 Analysis of normal vibrational frequencies of $[Ni(CO)_3F]^-$ in terms of local vibrational frequencies, calculated with M06/aug–cc–pVTZ [274]. (**a**) Adiabatic connection scheme (ACS) for $[Ni(CO)_3F]^-$ showing how the three equivalent local vibrational CO modes $\omega^a(5,6,7)$ are transformed into the A_1 normal mode ω_{18} and the two degenerate E normal modes ω_{16} and ω_{17} by switching on the masses via the perturbation parameter λ. (**b**) Decomposition of the 18 normal vibrational modes of $[Ni(CO)_3F]^-$ into 18 local vibrational modes. Each of the 18 normal mode vectors $\mathbf{d}_\mu$ is represented by a bar (mode numbers are given at the top of each bar, symmetry, and calculated frequencies at the bottom of each bar). Each $\mathbf{d}_\mu$ vector is decomposed in terms of 18 local mode vectors $\mathbf{a}_n$. The local mode parameters are presented in a form of a color code (right side of diagram; for numbering of atoms, see diagram in the lower right corner). Contributions larger than 5% are given within the partial bars representing a local mode

Table 1 Characterization of the 18 normal modes μ of $[Ni(CO)_3F]^-$ in terms of local mode contributions, calculated at the M06/aug–cc–pVTZ level of theory

Mode	Local mode contributions in percentage
18	63.9% (C3-O6, C4-O7), 32.0% 4.1% Ni-C
17	48.0% C3-O6, 48.0% C4-O7
16	64.0% C2-O5, 16.0% C4-O7, 16.0% C3-O6
15	33.9% Ni1-C2, 20.0% Ni1-C3-O6 (y), 19.9% Ni1-C4-O7 (y), 8.5% Ni1-C4, 8.5% Ni1-C3
14	25.2% Ni1-C2-O5 (x), 22.6% Ni1-C3, 22.6% Ni1-C4, 11.5% (C2-Ni1-C3, C2-Ni1-C4), 6.9% Ni1-C3-O6 (y), 6.9% Ni1-C4-O7 (y)
13	53.0% (Ni1-C3-O6 (x), Ni1-C4-O7 (x)), 26.6% Ni1-C2-O5 (y)
12	55.9% Ni1-C2, 14.0% Ni1-C3, 14.0% Ni1-C4
11	38.7% Ni1-C4, 38.7% Ni1-C3, 6.8% Ni1-C2-O5 (x)
10	52.3% (Ni1-C3, Ni1-C4), 26.1% Ni1-C2, 16.7% Ni1-F8
9	91.0% Ni1-F8
8	36.0% Ni1-C2-O5 (y), 18.0% (Ni1-C3-O6 (x), Ni1-C4-O7 (x)), 11.8% Ni1-C2, 8.6% Ni1-C3-O6 (y), 8.5% Ni1-C4-O7 (y), 6.7% F8-Ni1-C2
7	29.0% Ni1-C3-O6 (x), 29.0% Ni1-C4-O7 (x), 19.1% (Ni1-C3, Ni1-C4), 10.7% (F8-Ni1-C3, F8-Ni1-C4), 8.7% Ni1-C2-O5 (x)
6	33.9% Ni1-C2-O5 (x), 33.2% Ni1-C3-O6 (y), 33.0% Ni1-C4-O7 (y)
5	26.8% F8-Ni1-C2, 14.6% Ni1-C4-O7 (y), 14.5% Ni1-C3-O6 (y), 13.6% Ni1-C2-O5 (y), 13.3% (F8-Ni1-C3, F8-Ni1-C4)
4	36.6% (F8-Ni1-C3, F8-Ni1-C4), 23.2% (C2-Ni1-C3, C2-Ni1-C4), 18.5% (Ni1-C3-O6 (x), Ni1-C4-O7 (x)), 15.6% Ni1-C2-O5 (x)
3	36.4% (Ni1-C3-O6 (x), Ni1-C4-O7 (x)), 18.5% Ni1-C2-O5 (y), 17.1% (C2-Ni1-C3, C2-Ni1-C4), 16.4% (F8-Ni1-C3, F8-Ni1-C4), 8.4% F8-Ni1-C2
2	28.4% F8-Ni1-C2, 14.8% Ni1-C2-O5 (y), 14.5% (F8-Ni1-C3, F8-Ni1-C4), 8.2% C2-Ni1-C4, 8.2% C2-Ni1-C3, 7.3% Ni1-C4-O7 (y), 7.3% Ni1-C3-O6 (y)
1	35.1% (C2-Ni1-C3, C2-Ni1-C4), 30.3% (F8-Ni1-C3, F8-Ni1-C4), 15.9% (Ni1-C3-O6 (x), Ni1-C4-O7 (x)), 8.8% Ni1-C2-O5 (x)

The numbering of atoms is given in Fig. 6

substituents, and those with bulky substituents (sterically hindered phosphines, open black circles). It also has to be noted that while some of the relationships shown in Fig. 7 show the right trend, i.e., a stronger NiL bond, leads to a weaker CO bond, others predict an increase of the CO bond strength with increasing NiL bond strength. This contradicts Tolman's assumption that an increase of the electron density at the metal atom leads to increased CO π-back donation leading to an increased population of the CO anti-bonding π-orbital and a weakening of the CO bond that can be identified by a lower CO stretching frequency.

Overall, the scattering of data point is too large to derive any reliable mode of prediction. The obvious success of TEP studies reported in the literature is more a result of restricting the studies to a smaller set of chemically similar complexes (often <20). However, the comprehensive study of Setiawan and co-workers [274] clearly reveals that a more general application of the TEP is rather questionable, indicating that Tolman's bonding model is oversimplified and cannot capture the full complexity of ML bonding as shown in Fig. 1. Therefore, this bonding model has to

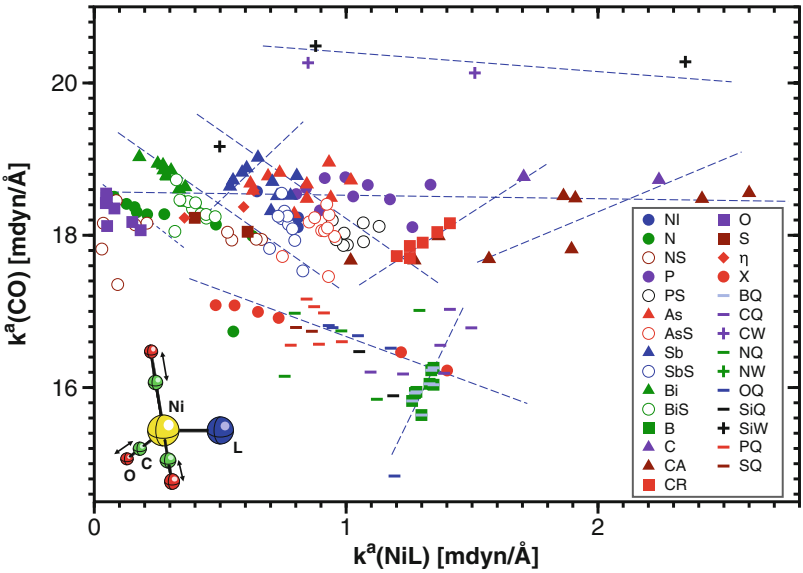

Fig. 7 There is no general relationship between the TEP and the intrinsic ML bond strength [274]. Some possible relationships are indicated by dashed blue lines. Each group of ligands is indicated by a colored symbol: NI, nitrogen and cyano; N, amines; NS, amines with steric hindrance; P, phosphines; PS, phosphines with steric hindrance; As, arsines; AsS, arsines with steric hindrance; Sb, stilbines; SbS, stilbines with steric hindrance; Bi, bismuthines; BiS, bismuthines with steric hindrance; B, boron compounds; C, carbonyl, thiocarbonyl; CA, carbenes; CR, Arduengo carbenes; O, water and ethers; S, thioethers; η, haptic ligands; X, halogens; BQ, boron anions; CQ, carbanions; CW, carbocations; NQ, nitronium anions; NW, nitronium cations; OQ, hydroxides; SiQ, silicon anions; SiW, silicon cations; PQ, phosphonium anions; SQ, thiohydrides. Calculated with M06/aug-cc-pVTZ. Reproduced from Ref. [131] with permission of the Royal Society of Chemistry

be strongly revised to capture the true electronic coupling between ML and CO bond strengths. Of course one has to say in Tolman's defense that he chose the A_1 symmetrical CO stretching frequency for practical reasons, because it could be easily measured in the 1960s and 1970s in nearly all cases, while at that time there was no access to the low-frequency ML vibrations.

5 The Metal–Ligand Electronic Parameter (MLEP)

In view of the recent advances in terahertz spectroscopy [277–280] or depolarized Raman scattering [281, 282], far-infrared absorptions down to 40 cm^{-1} can be measured nowadays. Therefore, there is no longer a problem to measure ML stretching frequencies. For example, the NiL stretching frequencies of the set of 181 [$NiCO_3L$] complexes range from 100 cm^{-1} for L = $N(C_6F_5)_3$ to 1,600 cm^{-1} for L = H [274]. Also the calculation of reliable vibrational frequencies even for larger systems has become feasible and more or less routine with today's computer

hardware and advanced quantum chemical software [283–285]. This has opened the avenue for assessing the ML bond strength directly from the analysis of the ML bond without making a detour around the CO bonds. The local mode stretching force constant k^a(ML) provides the perfect tool, which can be derived from experimental and/or calculated normal vibrational frequencies.

5.1 Relative Bond Strength Order (BSO)

Once the local ML stretching force constants k^a(ML) have been determined, one can simplify their comparison by translating the force constants into bond strength orders (BSO) n; most chemists are more acquainted with [75, 246, 259, 286]. This can be accomplished with Kraka, Larsson, and Cremer's extension of the Badger rule [246, 287], which states that the strength of a bond correlates with the frequency of its vibrational mode and vice versa in a form of a power relationship. Badger's original rule was derived for diatomic molecules using the bond length as measure of bond strength [287]. Kraka, Larsson, and Cremer showed that utilizing local stretching force constants and replacing bond lengths by BSO n values, the Badger rule can be generalized and in this way applied to the bonds of polyatomic molecules including different bonds between atoms of the same period. This has led to the power relationship shown in Eq. 13, transforming local mode stretching force constants into BSO n values to be used as more convenient bond strength descriptors, i.e., instead of defining the MLEP as the local mode stretching force constant k^a(ML), one can also define the MLEP as the BSO n(ML).

$$\text{BSO} \quad n = a(k^a)^b \tag{13}$$

The constants a and b in Eq. 13 can be determined via two reference compounds with known k^a values and the requirement that for a zero force constant k^a the corresponding BSO n value is also zero. Reference molecules and target molecules should be described with the same model chemistry (i.e., method/basis set) to guarantee that the BSO n values compare well.

It is straightforward to identify reference compounds for most covalent bonds being composed of main group atoms; e.g., for CC bonds, one can take the single bond in ethane and the double bond in ethylene with BSO n values of 1 and 2, respectively [286]. However, it is more difficult to find suitable reference bonds for non-covalent and/or transition metal bonds, which we solved in recent work [131, 274] by referring to Mayer or Wiberg bond orders [288, 289]. In the case of the ML bond in $[Ni(CO)_3L]$ complexes, we used as suitable reference bonds the CuC bond of $CuCH_3$ as a bond close to a single bond and the NiC bond in $NiCH_2$ close to a double bond. To quantify the single and double bond character, Mayer bond orders for these molecules were calculated to be n(Mayer,CuC) = 0.848 and n(Mayer, NiC) = 1.618, which corresponds to a ratio of 1.00:1.908. Utilizing the scaled Mayer bond orders of 1 for the CuC bond of $CuCH_3$ and 1.908 for the NiC bond in $NiCH_2$,

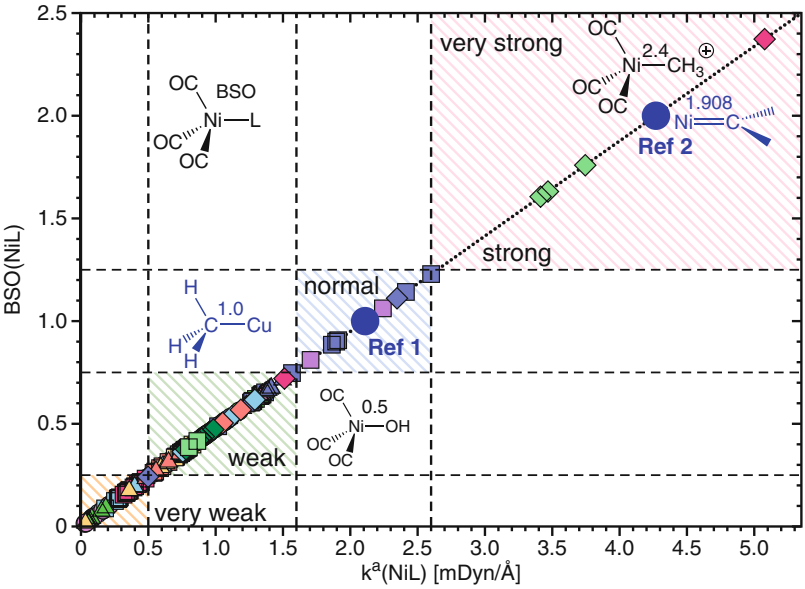

Fig. 8 BSO n(NiL) values of the NiL bonds for the set of 181 [Ni(CO)$_3$L] compounds, obtained with the power relationship BSO $n = 0.480\ (k^a)^{0.984}$ utilizing stretching force constant k^a(NiL). Calculated at the M06/aug-cc-pVTZ level of theory. For the derivation of the power relationship, see text. Regions of very weak, weak, normal, strong, and very strong NiL bonds are indicated by colored shading. The two reference molecules $CuCH_3$ with BSO $n = 1$ and $NiCH_2$ with BSO $n = 1.908$ are given in blue color. Reproduced from Ref. [131] with permission of the Royal Society of Chemistry

constants $a = 0.480$ and $b = 0.984$ were obtained for Eq. 13 (calculated at the M06/aug-cc-pVTZ level of theory) leading to the BSO n(NiL) values shown in Fig. 8 [131, 274]. There is a noticeable spread of BSO n values including very weak NiL bonds with almost zero bond order and very strong NiL bonds with bond orders of almost 2.5. This shows that the set of 181 [Ni(CO)$_3$L] complexes was well chosen, covering the breadth of possible NiL bonds. In the following, we will analyze the MLEPs represented by the BSO n(NiL) values for some groups of closely related ligands separately to highlight those electronic factors, which either increase or decrease the intrinsic NiL bond strength. A full report of this discussion can be found in Ref. [274].

5.2 *Intrinsic Strength of Nickel–Phosphine Bonding*

In Fig. 9, the BSO n values of 20 phosphines are compared including both normal trialkyl phosphines, phosphines with electronegative substituents, and those with bulky substituents. The BSO n values vary from 0.38 to 0.64, thus indicating that nickel–phosphine bonding is a relative soft bonding, resulting primarily from the σ-donor capacity of the phosphine that increases the number of Ni valence electrons to

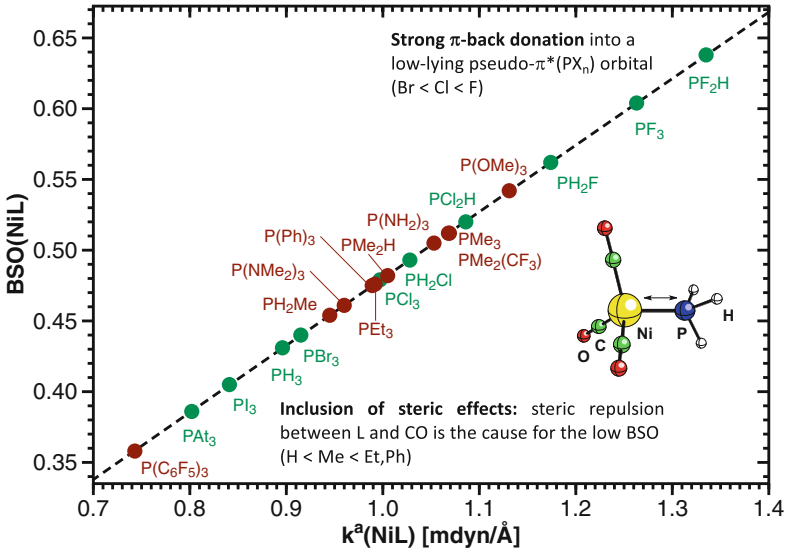

Fig. 9 BSO n(NiP) values of nickel–tricarbonyl–phosphine complexes $[R_3PNi(CO)_3]$ given as a function of the local stretching force constants k^a (NiP). Calculated at the M06/aug-cc-pVTZ level of theory. Halogenated phosphines (including PH_3) are given in green color and all others in brown color. Reproduced from Ref. [131] with permission of the Royal Society of Chemistry

18. As the H atoms in phosphine PH_3 are more electronegative than P, the σ-donor capacity of phosphine is reduced, and a BSO n value of just 0.43 results.

If the σ-donor capacity of the phosphine ligand is further reduced by electronegative substituents, the BSO n should become smaller. However, Fig. 9 reveals that the BSO n values of the Ni–P bond increase in the order $PAt_3 < PI_3 < PH_3 < PBr_3 < PCl_3 < PF_3$. For L = PF_3, one of the largest BSO n values (0.604) is found [274]. σ-bonding should increase from F (electronegativity $\chi = 4.10$ [290, 291]) to Cl(2.83), Br(2.74), H(2.20) $\sim$ I(2.21), and At(1.90), i.e., opposite to the observed trend. Obviously, there must be another effect, i.e., π-back donation, to the trihalogenophosphine, decisively overruling σ-donation.

This can be explained by considering that PF_3 has low-lying pseudo-$\pi^\star(PF_3)$ orbitals that can obtain negative charge from the Ni 3d-lone pair orbital, as shown in Fig. 1f, so that the Ni–P bond is strengthened despite the reduced σ-donor ability of PF_3. Delocalization of the Ni 3d-lone pair into a low-lying pseudo-$\pi^\star(PX_3)$ orbital decreases with the electronegativity of X from F to At as the energy of the pseudo-$\pi^\star(PX_3)$ orbital (X = F, Cl, Br, I, At) increases, and the overlap between the Ni 3d-orbital involved and the 3p$\pi(P)$-orbital contributing to the $\pi^\star(PX_3)$ orbital decreases. The 3p$\pi(P)$ coefficient of the $\pi^\star(PX_3)$ orbital is large if the PX bond polarity is large, i.e., larger electronegativity of X implies larger overlap, stronger back donation to the ligand, and thereby a stronger Ni–P bond. Hence, back donation to L decreases in the series F, Cl, Br, H $\sim$ I, At. One has to also consider a possible π-donor activity of the ligand involving an occupied pseudo-π orbital, as shown in Fig. 1e, provided the orbital energy is in the range of that of the Ni 3d-orbital leading

to sufficient overlap. Apart from that, 4e repulsive interaction with the occupied Ni 3d-orbitals is also possible.

Other effects such as steric bulk (increasing from PH_3 to PAt_3 and thereby weakening the Ni–L bond) or the relativistic contraction of the 5s(I),5p(I) or 6s (At),6p(At) orbitals, which leads to a smaller 3pπ(P) coefficient in the pseudo-$\pi^\star(PX_3)$ orbital and reduced back donation from Ni to L, also play a role. These effects cannot be captured by the TEP, which decreases from 2,140 (PF_3) to 2,135 (PCl_3), 2,133 (PBr_3), 2,129 (PI_3), and 2,127 cm^{-1} (PAt_3), thus suggesting an increase rather than decrease of the Ni–L bond strength. The unusually strong Ni–P bond for the PF_2H ligand (BSO $n = 0.638$, Fig. 9) is the result of a favorable compromise between a limited weakening of the σ-donation effect due to just two electronegative F substituents and still strong π-back donation into the pseudo-$\pi^\star(PHF_2)$ orbitals.

5.3 Special Role of Carbene Ligands

A prominent example of the increasing popularity of the TEP has been its application to transition metal complexes containing as ligand an N-heterocyclic carbene (NHC) [135, 137, 292, 293]. In recent reviews on N-heterocyclic carbene (NHC), Nelson and Nolan [294] and Dröge and Glorius [295, 296] discussed the TEP as a tool for experimentalists who investigate the electronic properties of metal–NHC complexes. For the purpose of studying the bonding properties of NHC ligands, usually the *cis*-[MCl(CO)$_2$ (NHC)] M = Rh, Ir model complexes are synthesized, because of the toxicity of the corresponding [Ni(CO)$_3$ (NHC)] complexes [294–297]. Using linear regression schemes proposed by Dröge and Glorius [296], TEP values obtained from different metal complexes can be correlated. This has led to a large compilation of TEP data for hundreds of NHC ligands, all using the same TEP scale. TEP values for NHCs generally stretch from 2,030 cm^{-1} for electron-rich NHCs to 2,060 cm^{-1} for electron-poor NHCs [294–296]. This seems to be a small range of TEP values, considering the large variety and complexity of NHC compounds stretching from NHCs with extended poly-aromatic substituents [176]; planar chiral imidazopyridinium-based NHCs, which can function as Lewis acids and ligands for transition metal complexes [185], nano-sized Janus *bis*-NHC ligands based on a quinoxalinophenanthrophenazine core [298], and NHCs with O-functionalized triazole backbones [299] and to cyclic alkyl amino carbenes as strongly donating ligands at the lower end of the NHC-TEP scale [183].

Singlet carbenes possess a lone pair for σ-donation and an empty $p\pi$-orbital for accepting negative charge from Ni. As shown in Fig. 1c, d, the full effect of these interactions cannot be captured by the TEP focusing just on the CO bonds. However, the data shown in Fig. 10 reveals that the BSO n(ML) recover the full effect. The BSO value of L = CH_2 is with 1.229 the largest of all neutral ligands included in the set of 181 [Ni(CO)$_3$L] complexes. Replacement of the H atoms by hyperconjugative or π-donor substituents $R = R'$ leads to a reduction of the NiC bond strength: R=CH_2 group (vinylidene; 1.142), Me (0.900), Cl (0.907), F (0.885), OMe (0.653), NH_2

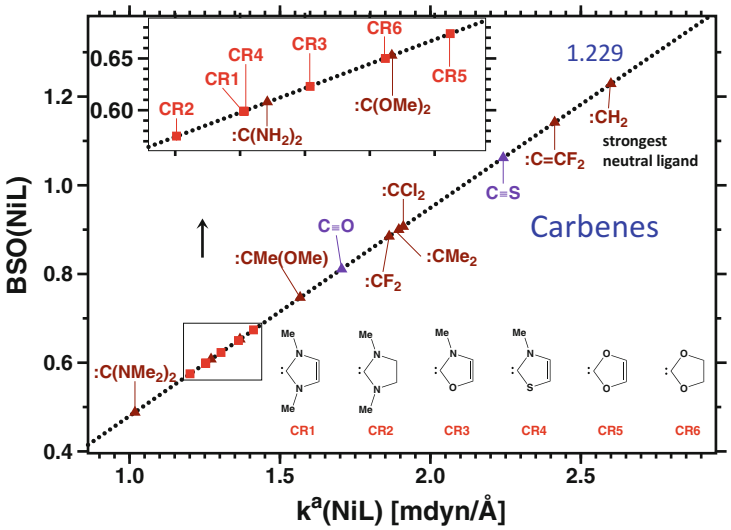

Fig. 10 BSO n(NiC) values of carbene–nickel–tricarbonyl [$R_2CNi(CO)_3$] given as a function of the local stretching force constants k^a(NiC). $Ni(CO)_4$ and Ni(CO)3CS complexes are also included (purple color) for comparison. Normal carbenes (brown color) are distinguished from Arduengo carbenes (red color). The clustering of data points in the region $0.57 < \text{BSO } n < 0.68$ is enlarged in the insert. Calculated at the M06/aug-cc-pVTZ level of theory. Reproduced from Ref. [274] with permission of the American Chemical Society

(0.608), and NMe_2 (0.488). Bulky groups lower the BSO value effectively because of the relatively small NiC bond length (1.9–2.0 Å). Noteworthy is that the CO and CS ligand lead to BSO values of 0.811 and 1.062. They are comparable in their NiC bond strength to that of substituted carbenes. Arduengo-type carbenes, which can form a delocalized 6π-system, withdraw negative charge from Ni, thus increasing the strength of the Ni–C bond. For five-membered rings with O atoms in α-position, the withdrawal is stronger (BSO $n = 0.674$ for CR5, Fig. 10) than for those with N atoms (BSO $n = 0.599$ for CR1, Fig. 10). It is interesting to note that the comparison of k^a(CO) and k^a(NiC) values for Arduengo carbenes shown in Fig. 7 suggests a reverse rather than inverse CO–NiC relationship for this group of ligands. This explains the reported failures of describing MC bonding of Arduengo carbenes on the basis of the TEP [139, 177, 218, 220, 300–303].

5.4 *Ionic Ligands*

As shown in Fig. 11, the methylidyne cation CH^+, which has a σ-lone pair and two empty $p\pi$-orbitals for back donation has the strongest NiL bond (BSO $n = 2.373$) of all 181 [$Ni(CO)_3L$] complexes investigated by Setiawan and co-workers [274].

In comparison, the methyl cation has a BSO n of just 0.720 and the t-butyl cation an even smaller BSO n value of 0.409. In the first case, the lowering of the BSO

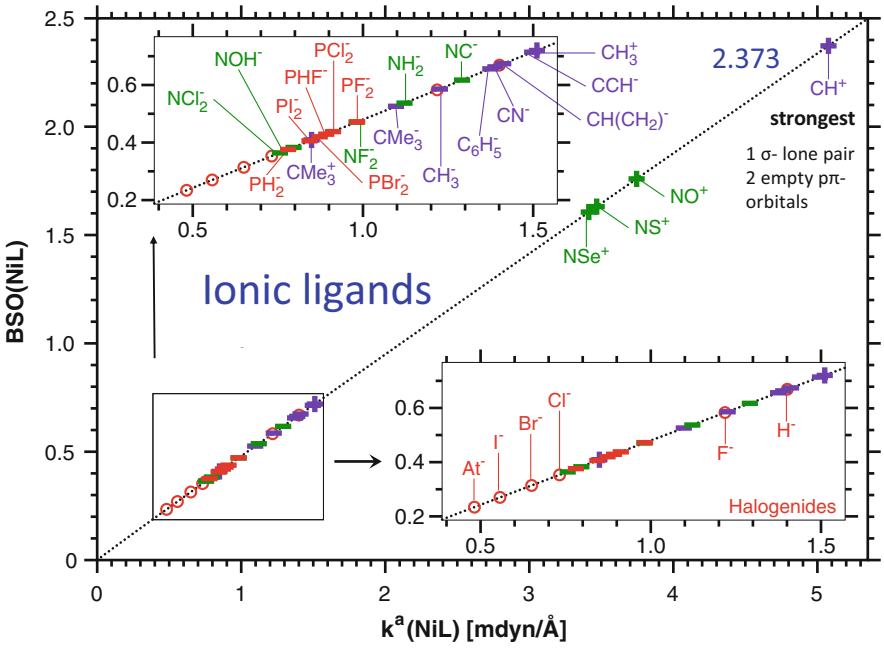

Fig. 11 NiC (purple), NiN (green), and NiP (red) BSO n values of ionic ligands are given as a function of the local stretching force constants k^a (NiL). The clustering of data points in the region $0.25 < \text{BSO} < 0.75$ is enlarged in two inserts, where the insert in the lower right corner features the halogenide anions (red open circles). Calculated at the M06/aug-cc-pVTZ level of theory. Reproduced from Ref. [274] with permission of the American Chemical Society

value is due to the missing σ-lone pair electrons whereas in the second case, the steric bulk of the ligand hinders the acceptance of negative charge from Ni.

Compared to the cationic ligands, variation of the BSO n values of the anionic ligands is much smaller. The halogenide anion X^- shows some interesting trends. Unexpectedly, the NiF bond strength is larger than that of all other halogenide anions (BSO $n = 0.583$) despite a small NiF distance R(NiF) of 1.991 Å, which should lead to destabilization because of lone pair–lone pair repulsion between Ni and F^-. If lone pair–lone pair repulsion is absent as in the case of the hydride anion, the BSO n value increases to 0.669 ($R = 1.579$ Å) [274]. The large BSO $n(NiF^-)$ value is obviously due to the delocalization of F^- lone pair electrons. In the case of halogenide ligands with higher atomic numbers, delocalization into an empty Ni valence orbital is reduced because of smaller overlap and a raise in the lp(X) orbital energy. BSO n values for ligands of carbanionic character vary between 0.526 (CMe_3^-) and 0.714 (HCC^-), where steric interactions cause a decrease in the NiC bond strength. Amide and phosphide anions lead to less strongly bonded $[Ni(CO)_3L]$ complexes (see Fig. 11). Noteworthy is that PF_2^- is the most strongly bonded phosphide anion ligand, which again underlines the important role of π-back donation from a Ni 3d-orbital into the pseudo-$\pi^\star(PF_2)$-orbital.

5.5 Generalization of the MLEP

With a few exceptions, the TEP has been limited to the description of transition metal–carbonyl complexes. In contrast, the MLEP can be determined for any ML bond of any metal or transition metal complex, whether it contains CO ligands or not. In this way, the MLEP provides a unique measure of the intrinsic strength of any metal and/or transition metal bond including metal and transition metal atoms across the periodic table. In the following section, we will present two recent examples.

MLEP for Fe–H Interactions Makoś and co-workers investigated the strength of the H^- and H_2 interaction with the Fe atom of a [NiFe] hydrogenase mimic and how this interaction can be modulated by changing the Fe ligand in *trans* position relative to H^- and H_2 [262]. 17 different ligands were investigated at the BP86 level of theory [304, 305] using the cc-pVTZ basis set [276, 306]. The investigation included σ-donor ligands such as CH_3^-, $C2H_5^-$, NH_3, and H_2O, π−donor ligands such as Cl^-, F^-, and OH^-, and σ-donor/π–acceptor ligands such as CN^- and CO as shown in Fig. 12a. According to the comprehensive local mode analysis performed in this work, Fe–H interactions are strengthened by σ-donor or π-donor ligands and weakened by σ-donor/π-acceptor ligands. In contrast, the H–H bond of H_2 in complexes **B** is weakened by σ-donor or π-donor ligands and strengthened by σ-donor/π-acceptor ligands.

A new metal–ligand electronic parameter (MLEP) for Fe–H ligands was developed in this work, which can be generally applied to evaluate the Fe–H bond strength in iron complexes and iron hydrides. For the underlying Fe–H power relationship, the low-spin complex $[Fe(CO)_5]$ was used, in which one axial CO ligand was replaced by H_2 (reference 1) and by H^- (reference 2), respectively. The C_{3v} symmetric $[Fe(CO)_4H]$ complex led to a k^a(F–H) value of 1.954 mDyn/Å, and the C_s symmetric $[Fe(CO)_4H_2]$ complex led to a k^a(F–H) value of 1.024 mDyn/Å. As BSO n values for these two references, the corresponding Mayer bond orders [289] n (Mayer) 0.6454 and n(Mayer) 0.4775 were used, respectively. This led to the constants $a = 0.47225$ and $b = 0.46630$:

$$\text{BSO } n(\text{Fe} - \text{H}) = 0.47225 \left(k^a\right)^{0.46630} \tag{14}$$

In Fig. 12b, the MLEP(Fe–H) defined as BSO n(FeH) is shown for the 55 Fe–H bonds of complexes **A1**–**A17** and complexes **B1**–**B17**, FeH and FeH_2, together with the two reference compounds $[Fe(CO)_4H_2]$ and $[Fe(CO)_4H]$ [262]. MLEP values stretch over a range of 0.478 to 0.645 revealing that Fe–H_a bonds are generally weaker than Fe–H_b bonds in complexes **A1**–**A17** and that the Fe–H hydride bonds in complexes **B1**–**B17** are stronger than their complex **A** counterparts. As a first proof for the general applicability of the MLEP(Fe–H), Fig. 12b also includes two iron hydrides, the high-spin FeH_2 molecule, the only transition metal dihydride, which has been detected so far in the gas phase [307] with Fe–H bonds in the medium strong range, and the diatomic FeH molecule, one of the few molecules found in the Sun [308, 309]. FeH has been extensively studied by DeYonker and Allen

(a)

Complex A

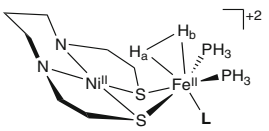

Complex B

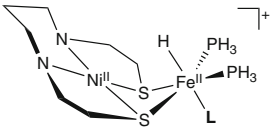

Ligand	SCN^-	CO	NO_2^-	CN^-	PH_3	ON	CH_3^-	$C_6H_5^-$	$C_2H_5^-$	C_2H_4	NH_3	H_2S	NCS^-	F^-	Cl^-	OH^-	H_2O
Complex **A**	**A1**	**A2**	**A3**	**A4**	**A5**	**A6**	**A7**	**A8**	**A9**	**A10**	**A11**	**A12**	**A13**	**A14**	**A15**	**A16**	**A17**
Complex **B**	**B1**	**B2**	**B3**	**B4**	**B5**	**B6**	**B7**	**B8**	**B9**	**B10**	**B11**	**B12**	**B13**	**B14**	**B15**	**B16**	**B17**

(b)

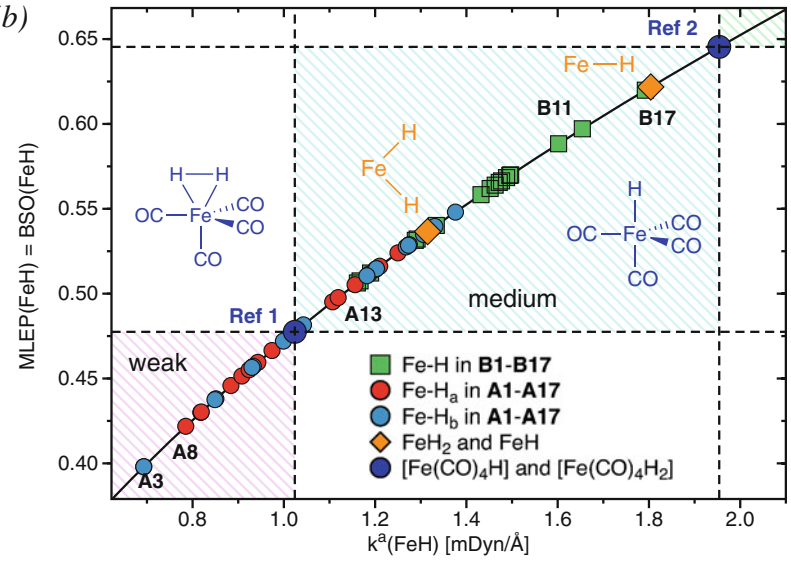

Fig. 12 Fe–H^- and Fe–H_2 interactions in a [NiFe] hydrogenase mimic. Calculated at the BP86/cc-pVTZ level of theory. Reproduced from Ref. [262] with permission of Springer. (**a**) [NiFe] complexes **A** and **B** and the corresponding ligands (**L**) investigated. (**b**) BSO n(FeH) values as a function of the corresponding local k^a(FeH) stretching force constants. Regions of weak, medium, and strong Fe–H bonds are indicated by colored shading. Fe–H bonds in compounds **B1**–**B17** as defined in Fig. 12a are shown as green squares, Fe–H_a bonds of complexes **A1**–**A17** are shown as light blue, and Fe–H_b bonds are shown as red dots. The two reference compounds, Ref 1 and Ref 2, are shown in blue color and the corresponding BSO n values as dark blue dots; FeH and FeH_2 are shown in orange color and the corresponding BSO n values as orange diamonds

[309]. The Fe–H bond of the lowest-lying $X^4\Delta$ state of the FeH molecule is as strong as the Fe–H bond in complex **B17**.

The results of Makoś and co-workers form a valuable basis for future [NiFe] hydrogenase-based catalyst design and fine-tuning, as well as for the development of efficient biomimetic catalysts for H_2 generation. Work is in progress to extend these studies to other Fe–H complexes of interest in catalysis [310–312] and as functional materials [313].

MLEP for Au–Au and Au–Zn Bonds in Gold Clusters The second example concerns the extension of the MLEP to characterize M–M bonds in gold clusters. Li,

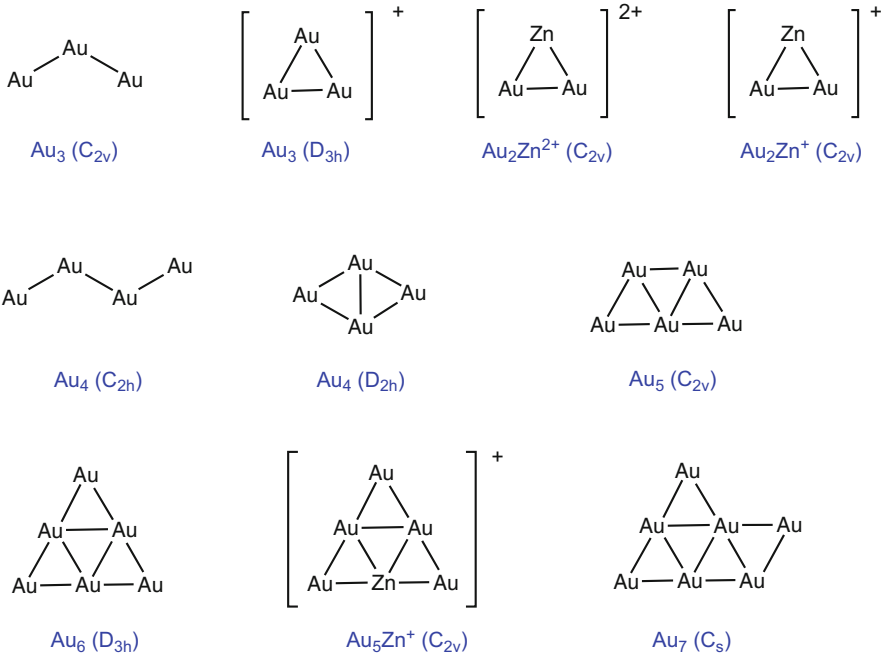

Fig. 13 Gold clusters investigated by Li, Oliveira, and co-workers [272]

Oliveira, and co-workers investigated the stability of small Au_m ($m = 4$–7) clusters including also two isoelectronic Au/Zn clusters, shown in Fig. 13, by analyzing their energetic, geometric, vibrational, magnetic, and electron density properties. This work led to a quantitative assessment of aromaticity and antiaromaticity based on local vibrational Au–Au and Au–Zn force constants, which led to a new understanding of the structure and stability of polycyclic gold clusters applying a new equivalent of Clar's Aromaticity Rule [273] based on local vibrational force constants [271, 272].

In the following section, we will focus on the characterization of the intrinsic Au–Au and Au–Zn bond strength determined by local mode force constants k^a(Au–Au) and k^a(Au–Zn), showing that the MLEP is a sensitive tool to differentiate between inner and peripheral bonds in clusters [272].

As suitable references for the corresponding BSO n values, the Au_2 dimer and the three-ring Au_3^+ were chosen. For the B3LYP level of theory [314] using the LANL2DZ basis set [315–317], k^a values of 1.567 and 0.833 mdyn/Å were obtained for the Au_2 dimer and the three-ring Au_3^+ and Mayer bond orders [289] of 0.610 and 1.032, respectively, leading to the power relationship shown in Eq. 15:

$$\text{BSO } n = 0.724\ (k^a)^{0.941} \tag{15}$$

The corresponding BSO n (Au–Au) and (Au–Zn) values are shown in Fig. 14 as a function of the Au–Au and Au–Zn local stretching force constants. As revealed by the data in Fig. 14, the strongest Au–Au bond is found for open form of Au_4 with

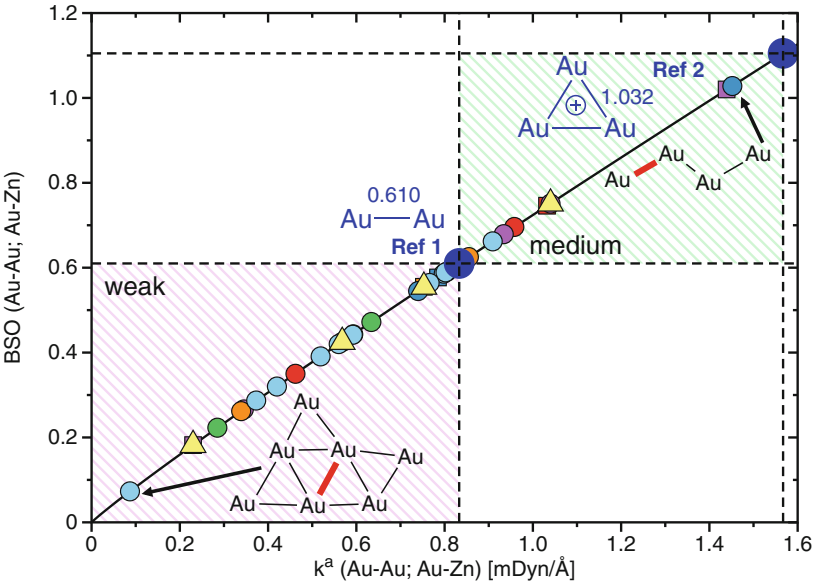

Fig. 14 BSO n(Au–Au) and BSO n(Au–Zn) values as a function of the corresponding local k^a(Au–Au) and k^a(Au–Zn) stretching force constants. Regions of weak and medium bonds are indicated by colored shading. Au–Au bonds are shown as dots, Au–Zn bonds as yellow squares. The two clusters with the weakest and the strongest Au–Au bond are shown. The two reference compounds Au_2 dimer (Ref 1) and the three-ring Au_3^+ (Ref 2) are shown in blue color and the corresponding BSO n values as blue dots. Calculated at the B3LYP/LANL2DZ level of theory

(C_{2v}) symmetry, and the weakest Au–Au bond is located inside the Au_7 cluster. This is in line with the comprehensive orbital and electron density analysis of Li, Oliveira, and co-workers [272]. They found that for the small Au_m clusters, a distorted three-ring is always possible if three-dimensional clusters are avoided. The use of three rings as building blocks leads to a steep increase in the number of bonding interactions that require electron-deficient bonding. This in turn enforces electron sharing between the three rings and a move of negative charge from the more central three rings to the peripheral three rings, so that the latter can adopt 3c–2e units of larger stability with relatively strong bonding on the outside and weak (electron-deficient) Au–Au bonds on the inside. This is reflected by the local stretching force constants and the associated BSO values, which can serve as a basis to predict the stability of larger gold clusters, which no longer might prefer a planar structure. It is important to consider, besides Clar's Rule for three rings [273], the stabilization via peripheral electron delocalization and the avoidance of other highly destabilized subunits such as the tetracyclic and bicyclic Au_4 or the hexacyclic Au_6. Work is in progress to provide a general rationale for the stability of larger gold clusters based on local Au–Au and Au–Zn force constants.

These two examples clearly show that the MLEP is a powerful tool to discuss the bond strength of ML bonds and beyond.

6 Conclusion and Outlook

The idea of inventing a simple spectroscopic means in a form of the symmetric CO stretching frequency (TEP) to describe the metal–ligand bond was appealing as it could be used to single out those ligands that can be easily replaced in the course of a catalytic reaction. This was an important step forward at a time where only CO but not ML stretching frequencies were accessible to vibrational spectroscopy. However, there are three fundamental problems that make the TEP questionable, which may be even a misleading parameter: (1) As shown in this article, the A_1 symmetric CO stretching frequency does not describe all aspects of the complex ML interactions, reflected by a redshift which is too low. (2) There is mode–mode coupling between CO and MC stretching vibrations that leads to coupling errors in the range of (20–200 cm^{-1}) [131, 274], which can be larger than the variation in the TEPs caused by different ligands L. (3) The relationship between ML bond strength and TEP, considered by Tolman as a key electronic feature of transition metal–carbonyl complexes $(CO)_nML_m$, is generally neither quantitatively nor qualitatively fulfilled, because the electronic ML bonding mechanism is much more complex than described by the TEP [130]. This leads to the following conclusions:

1. The basic idea of Tolman was and still is a valuable one. Vibrational spectroscopy, in the form of infrared, Raman, or the more modern terahertz spectroscopy, provides sensitive tools to describe the electronic structure of any transition metal complex or any catalyst in general. However, there is no longer a need to refer to the CO stretching vibration, since one can access nowadays the ML stretching vibration directly. There is only the necessity to convert measured normal mode frequencies into local mode frequencies and then derive all other local mode properties needed, especially the local stretching force constants that reflect in a universal way the intrinsic strength of any bond.
2. The local stretching force constants k^a(ML) can be easily converted into bond strength orders (BSO) n, which provide a useful ordering of chemical bonds according to their strength. If the BSO n is used as MLEP instead of k^a(ML), MLEP values can be easily compared from one ML bond type to the other. This procedure can be carried out with measured or calculated data, where in the former case a conversion from normal mode into local mode frequencies can be carried out using the procedure of Cremer and co-workers [76]. In addition, chemically meaningful reference molecules with known BSO n have to be utilized in order to determine the BSO n values from a power relationship. As shown in this work, Mayer bond orders are the best choice for metals and transition metals.
3. The MLEP covers all electronic effects of ML bonding including steric effects. Therefore, no Tolman cone angle is needed. However, steric effects can be isolated via local bending force constants and corresponding bending orders.

We are currently compiling a library of MLEP values for ML bonds across the periodic table, some of which are summarized in the Appendix. Work is also in progress to release of first open-source version of the local mode analysis program.

Acknowledgment We thank Dani Setiawan for providing us the data for the bending force constants and Daniel Sethio for his valuable comments and suggestions. This work was financially supported by the National Science Foundation, Grants CHE 1464906. We thank SMU for providing computational resources.

Appendix The appendix contains a compilation of local mode force constants k^a(ML) in mdyn/Å (blue color) and corresponding local mode frequencies ω^a in cm^{-1} (red color) for a series of metal/transition metal complexes, which are part of the MLEP library currently under construction. For Cr and some Ti complexes also, the $k^a(M\cdots\pi)$ and corresponding local mode frequencies $\omega^a(M\cdots\pi)$ are given, which can be calculated by using curvilinear coordinates (Figs. 15 , 16 , and 17).

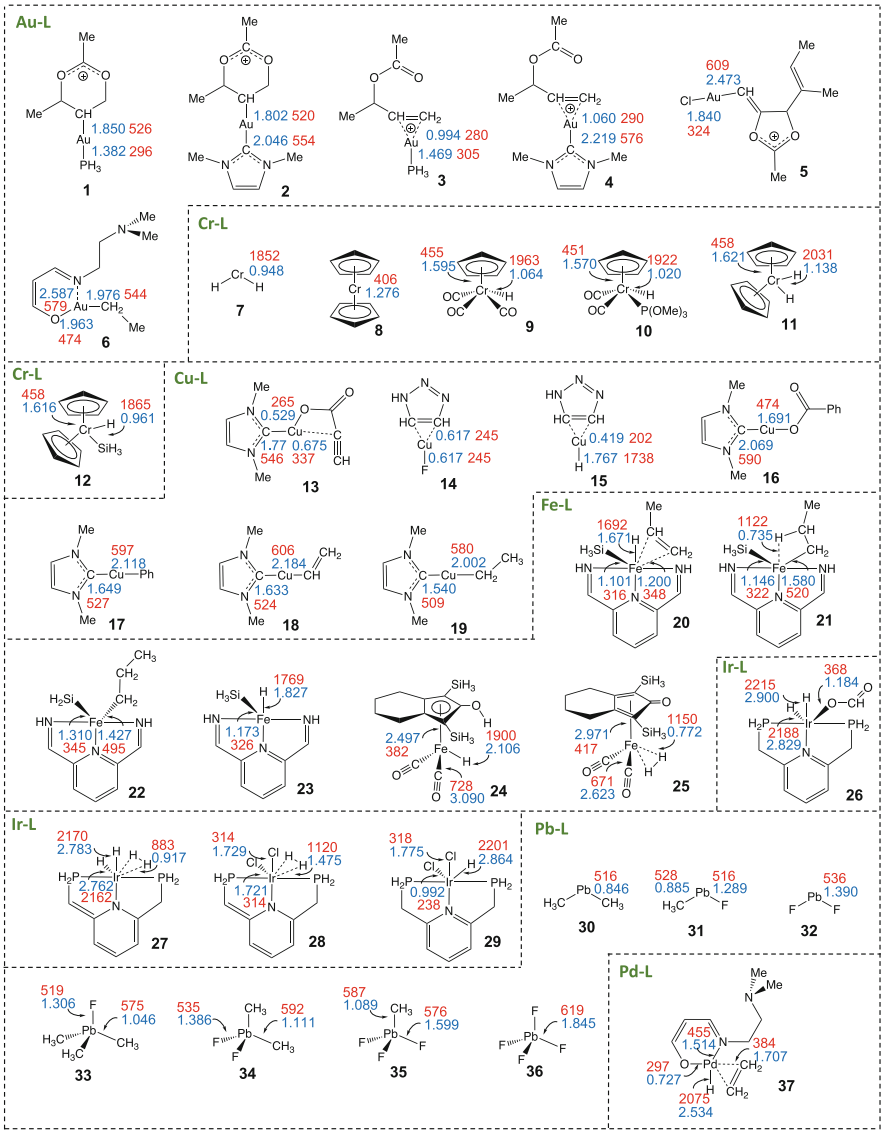

Fig. 15 Extract from the MLEP library, part 1

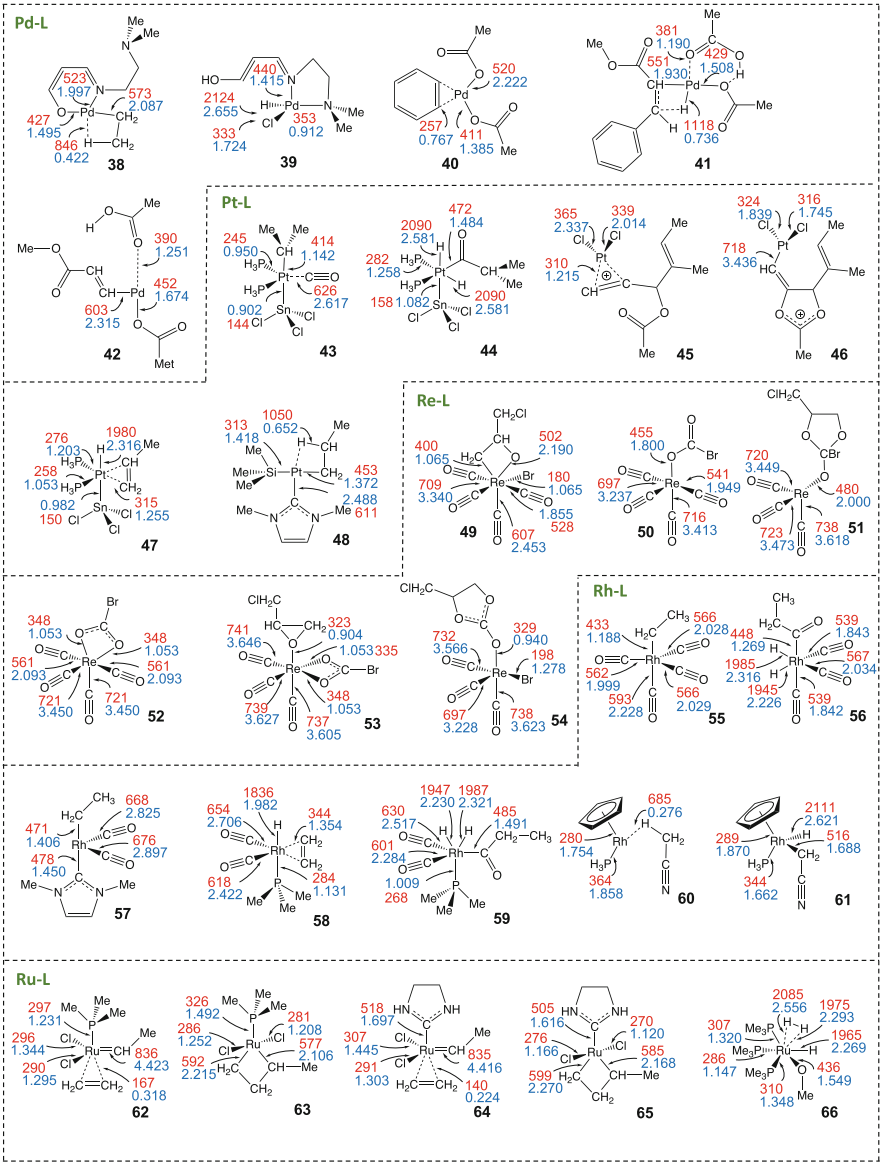

Fig. 16 Extract from the MLEP library, part 2

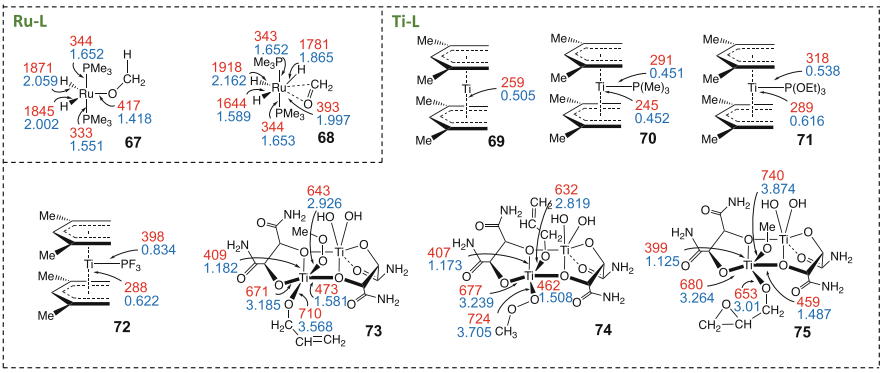

Fig. 17 Extract from the MLEP library, part 3

References

1. Seyferth D (2001) Organometallics 20:11488–11498
2. Crabtree RH (2019) The organometallic chemistry of the transition metals. Wiley, New York
3. Perez PJ (2019) Advances in organometallic chemistry: volume 71-72. Academic Press, New York
4. Eschenbroich C (2016) Organometallics. Wiley, New York
5. Hartwig J (2010) Organotransition metal chemistry: from bonding to catalysis. University Science Books, New York
6. Stradiotto M, Lundgren RJ (eds) (2016) Ligand design in metal chemistry – reactivity and catalysis. Wiley, New York
7. Beller M, Blaser HU (eds) (2012) Topics in organometallic chemistry 42: organometallics as catalysts in the fine chemical industry. Springer, Heidelberg
8. Maity B, Abe S, Ueno T (2019) Tailoring organometallic complexes into protein scaffolds. In: Advances in bioorganometallic chemistry. Elsevier, Amsterdam, pp 329–346
9. Brown CJ, Dean Toste F, Bergman RG, Raymond KN (2015) Chem Rev 115(9):3012–3035
10. Kam K, Lo W (eds) (2017) Inorganic and organometallic transition metal complexes with biological molecules and living cells. Academic Press, London
11. Dixneuf PH, Soulé JF (eds) (2019) Organometallics for green catalysis. Springer, New York
12. Macgregor SA, Eisenstein O (eds) (2016) Structure and bonding 167: computational studies in organometallic chemistry. Springer, Heidelberg
13. AB NM (2019) Nobel Prize in chemistry. https://www.nobelprize.org
14. Tan D, Garcia F (2019) Chem Soc Rev 48:2274–2292
15. Montero-Campillo M, Mo O, Yanez M, Alkorta I, Elguero J (2019) Adv Inorg Chem 73:73–121
16. Buchner MR (2019) Chem Eur J 25:12018–12036
17. Edelmann FT (2018) Coord Chem Rev 370:129–223
18. Walter O (2019) Chem Eur J 25:2927–2934
19. Tomas R, Karel S (2008) Phytochemistry 69:2927–2934
20. Dornsiepen E, Geringer E, Rinn N, Dehnen S (2019) Coord Chem Rev 380:136–169
21. Karimi B, Behzadnia H, Elhamifar D, Akhavan PF, Esfahani FK, Zamani A (2000) Synthesis 9:1399–1427
22. Schlosser M (ed) (2013) Organometallics in synthesis. Wiley, New York
23. Hartwig JF (2011) Nat Chem 3(2):99–101
24. Hartwig JF (2008) Nature 455:314–322

25. Newhouse T, Baran PS (2011) Angew Chem Int Ed 50:3362–3374
26. Boyt SM, Jenek NA, Hintermair U (2019) Dalton Trans 48:5107–5124
27. Zecchina A, Califano S (2017) The development of catalysis: a history of key processes and personas in catalytic science and technology. Wiley, New York
28. Paul CJK (ed) (2017) Contemporary catalysis: science, technology, and applications, Gld edn. Royal Society of Chemistry, London
29. Ruiz JCS (ed) (2017) Applied industrial catalysis. Arcler Press LLC, New York
30. Copyret C, Allouche F, Chan KW, Conley MP, Delley MF, Fedorov A, Moroz IB, Mougel V, Pucino M, Searles K, Yamamoto K, Zhizhko PA (2018) Angew Chem Int Ed 57:6398–6440
31. Samantaray MK, Pump E, Bendjeriou-Sedjerari A, D'Elia V, Pelletier JDA, Guidotti M, Psaro R, Basset JM (2018) Chem Soc Rev 47:8403–8437
32. González-Sebastián L, Morales-Morales D (2019) J Organomet Chem 893:39–51
33. Banach L, Gunka P, Zachara J, Buchowicz W (2019) Coord Chem Rev 389:19–58
34. Ye Z, Wayland BB (2013) Chapter 5 mechanistic aspects of living radical polymerization mediated by organometallic complexes. The Royal Society of Chemistry, London, pp 168–204
35. Allan LEN, Perry MR, Shaver MP (2012) Prog Polym Sci 37(1):127–156
36. Hurtgen M, Detrembleur C, Jerome C, Debuigne A (2011) Polym Rev 51(2):188–213
37. Poli R (2006) Angew Chem Int Ed 45(31):5058–5070
38. Braunecker WA, Matyjaszewski K (2007) Prog Polym Sci 32(1):93–146
39. Werlé C, Meyer K (2019) Organometallics 38(6):1181–1185
40. Bellini M, Bevilacqua M, Marchionni A, Miller HA, Filippi J, Grützmacher H, Vizza F (2018) Eur J Inorg Chem 2018(40):4393–4412
41. Ciobotaru IC, Polosan S, Ciobotaru CC (2019) Inorg Chim Acta 483:448–453
42. Wang RS, Chen LC, Yang H, Fu MA, Cheng J, Wu XL, Gao Y, Huang ZB, Chen XJ (2019) Phys Chem Chem Phys 21(47):25976–25981
43. Martínez-Calvo M, Mascareñas JL (2018) Coord Chem Rev 359:57–79
44. García-Álvarez J, Hevia E, Capriati V (2018) Chem Eur J 24:14854–14863
45. Trammell R, Rajabimoghadam K, Garcia-Bosch I (2019) Chem Rev 119:2954–3031
46. Campeau LC, Fogg DE (2019) Organometallics 38(1):1–2
47. Bauer EB, Haase AA, Reich RM, Crans DC, Kühn FE (2019) Coord Chem Rev 393:79–117
48. Parveen S, Arjmand F, Tabassum S (2019) Eur J Med Chem 175:269–286
49. Schatzschneider U (2019) Antimicrobial activity of organometal compounds. In: Advances in bioorganometallic chemistry. Elsevier, Amsterdam, pp 173–192. https://doi.org/10.1016/b978-0-12-814197-7.00009-1
50. Desnoyer AN, Love JA (2017) Chem Soc Rev 46:197–238
51. Chelucci G (2017) Coord Chem Rev 31:1–36
52. Li D, Li X, Gong J (2016) Chem Rev 116:11529–11653
53. Klein A, Sandleben A, Vogt N (2016) PNAS 86(4, SI):533–549
54. Guan W, Zeng G, Kameo H, Nakao Y, Sakaki S (2016) Chem Rec 16(5, SI):2405–2425
55. Julia-Hernandez F, Gaydou M, Serrano E, van Gemmeren M, Martin R (2016) Top Curr Chem 374:45–68
56. Augustine RL (2016) Catal Lett 146(12):2393–2416
57. Dean J, Tantillo GE (eds) (2016) Accounts of chemical research: computational catalysis for organic synthesis, vol 46. American Chemical Society, Washington
58. Bhaduri S, Mukesh D (2014) Homogenous catalysis. Wiley, New York
59. Durand DJ, Fey N (2019) Chem Rev 119(11):6561–6594
60. Ahn S, Hong M, Sundararajan M, Ess D, Baik M (2019) Chem Rev 119:6509–6560
61. Coley CW, Green WH, Jensen KF (2018) Acc Chem Res 51:6281–1289
62. von Lilienfeld OA (2018) Angew Chem Int Ed 57:4164–4169
63. Luo YR (2007) Comprehensive handbook of chemical bond energies. Taylor and Francis, Boca Raton
64. Moltved KA, Kepp KP (2018) J Chem Theory Comput 14(7):3479–3492

65. Kosar N, Ayub K, Gilani MA, Mahmood T (2019) J Mol Model 25(2):47–60
66. Morse MD (2018) Acc Chem Res 52(1):119–126
67. Fang Z, Vasiliu M, Peterson KA, Dixon DA (2017) J Chem Theory Comput 13(3):1057–1066
68. Lakuntza O, Besora M, Maseras F (2018) Inorg Chem 57:14660–14670
69. Cremer D, Kraka E (2010) Curr Org Chem 14:1524–1560
70. Kalescky R, Kraka E, Cremer D (2014) Int J Quantum Chem 114:1060–1072
71. Kalescky R, Zou W, Kraka E, Cremer D (2014) J Phys Chem A 118:1948–1963
72. Oliveira V, Kraka E, Cremer D (2016) Inorg Chem 56:488–502
73. Setiawan D, Sethio D, Cremer D, Kraka E (2018) Phys Chem Chem Phys 20:23913–23927
74. Sethio D, Oliveira V, Kraka E (2018) Molecules 23:2763
75. Kraka E, Cremer D (2009) ChemPhysChem 10:686–698
76. Cremer D, Larsson JA, Kraka E (1998) New developments in the analysis of vibrational spectra on the use of adiabatic internal vibrational modes. In: Parkanyi C (ed) Theoretical and computational chemistry. Elsevier, Amsterdam, pp 259–327
77. Konkoli Z, Larsson JA, Cremer D (1998) Int J Quantum Chem 67:11–27
78. Konkoli Z, Cremer D (1998) Int J Quantum Chem 67:29–40
79. Kaupp M, Danovich D, Shaik S (2017) Coord Chem Rev 344:355–362
80. Wu D, Dong C, Zhan H, Du XW (2018) J Phys Chem Lett 9(12):3387–3391
81. Lai W, Li C, Chen H, Shaik S (2012) Angew Chem Int Ed 51:5556–5578
82. Stasyuk OA, Sedlak R, Guerra CF, Hobza P (2018) J Chem Theory Comput 14(7):3440–3450
83. Levine DS, Head-Gordon M (2017) PNAS 114(48):12649–12656
84. Andrés J, Ayers PW, Boto RA, Carbó-Dorca R, Chermette H, Cioslowski J, Contreras-García J, Cooper DL, Frenking G, Gatti C, Heidar-Zadeh F, Joubert L, Martín Pendás Á, Matito E, Mayer I, Misquitta AJ, Mo Y, Pilmé J, Popelier PLA, Rahm M, Ramos-Cordoba E, Salvador P, Schwarz WHE, Shahbazian S, Silvi B, Solà M, Szalewicz K, Tognetti V, Weinhold F, Zins ÉL (2019) J Comput Chem 40:2248–2283
85. Zou W, Kalescky R, Kraka E, Cremer D (2012) J Chem Phys 137:084114
86. Wilson EB, Decius JC, Cross PC (1955) Molecular vibrations. The theory of infrared and raman vibrational spectra. McGraw-Hill, New York
87. Kratzer A (1920) Z Physik 3:289–307
88. Kratzer A (1925) Phys Rev 25:240–254
89. Mecke R (1925) Z Physik 32:823–834
90. Morse PM (1929) Phys Rev 34:57–64
91. Badger RM (1935) Phys Rev 48:284–285
92. Allen HS, Longair AK (1935) Nature 135:764–764
93. Badger RM (1935) J Chem Phys 3:710–715
94. Huggins ML (1935) J Chem Phys 3:473–479
95. Huggins ML (1936) J Chem Phys 4:308–312
96. Sutherland GBBM (1938) Proc Indiana Acad Sci 8:341
97. Sutherland GBBM (1940) J Chem Phys 8:161–165
98. Clark CHD, Webb KR (1941) Trans Faraday Soc 37:293–298
99. Wu CK, Yang C (1944) J Phys Chem 48:295–303
100. Linnett JW (1945) Trans Faraday Soc 41:223–232
101. Gordy W (1946) J Chem Phys 14:305–321
102. Wu CK, Chao SC (1947) Phys Rev 71:118–121
103. Guggenheimer KM (1950) Discuss Faraday Soc 9:207–222
104. Herzberg G (1950) Spectra of diatomic molecules, 2nd edn. D. Van Nostand Co. Inc., Princeton
105. Siebert H (1953) Z Anorg Allg Chem 273:170–182
106. Lippincott ER, Schroeder R (1955) J Chem Phys 23:1131–1142
107. Jenkins HO (1955) Trans Faraday Soc 51:1042–1051
108. Varshni YP (1958) J Chem Phys 28:1078–1081
109. Varshni YP (1958) J Chem Phys 28:1081–1089

110. Hershbach DR, Laurie VW (1961) J Chem Phys 35:458–463
111. Johnston HS (1964) J Am Chem Soc 86:1643–1645
112. Ladd JA, Orville-Thomas WJ, Cox BC (1964) Spectrochim Acta 20:1771–1780
113. Ladd JA, Orville-Thomas WJ (1966) Spectrochim Acta 22:919–925
114. Taylor WJ, Pitzer KS (1947) J Res Natl Bur Stand 38:1
115. Decius JC (1953) J Chem Phys 21:1121
116. Cyvin SJ, Slater NB (1960) Nature 188:485–485
117. Decius J (1963) J Chem Phys 38:241–248
118. Cyvin SJ (1971) Theory of compliance matrices. In: Molecular vibrations and mean square amplitudes. Universitetsforlaget, Oslo, pp 68–73
119. Strohmeier W, Guttenberger J (1964) Chem Ber 97:1871–1876
120. Strohmeier W, Müller F (1967) Z Naturforsch 22B:451–452
121. Fischer R (1960) Chem Ber 93:165–175
122. Horrocks Jr WD, Taylor RC (1963) Inorg Chem 2:723–727
123. Hecke GRV, Horrocks Jr WD (1966) Inorg Chem 5:1960–1968
124. Cotton FA, Zingales F (1962) Inorg Chem 1:145–147
125. Kraihanzel CS, Cotton FA (1963) Inorg Chem 2:533–540
126. Cotton FA (1964) Inorg Chem 3:702–711
127. Cotton FA, Musco A, Yagupsky G (1967) Inorg Chem 6:1357–1364
128. Tolman CA (1970) J Am Chem Soc 92:2953–2956
129. Tolman CA (1972) Chem Soc Rev 1(3):337–353
130. Tolman CA (1977) Chem Rev 77(3):313–348
131. Cremer D, Kraka E (2017) Dalton Trans 46:8323–8338
132. Huber KP, Herzberg G (1979) Molecular spectra and molecular structure, IV. Constants of diatomic molecules. Van Nostrand Reinholdl, New York
133. Roodt A, Otto S, Steyl G (2003) Coord Chem Rev 245:121–137
134. Kühl O (2005) Coord Chem Rev 249(5-6):693–704
135. Arduengo III A, Harlow R, Kline M (1991) J Am Chem Soc 113:361–363
136. Arduengo III A, Dias R, Harlow R, Kline M (1992) J Am Chem Soc 114:5530–5534
137. Anthony JA (1999) Acc Chem Res 32:913–921
138. Perrin L, Clot E, Eisenstein O, Loch J, Crabtree RH (2001) Inorg Chem 40:5806–5811
139. Gusev DG (2009) Organometallics 28(3):763–770
140. Gusev DG (2009) Organometallics 28(22):6458–6461
141. Tonner R, Frenking G (2009) Organometallics 28(13):3901–3905
142. Zobi F (2009) Inorg Chem 48:10845–10855
143. Fianchini M, Cundari TR, DeYonker NJ, Dias HVR (2009) Dalton Trans 12(12):2085–2087
144. Mathew J, Suresh CH (2010) Inorg Chem 49:4665–4669
145. Kalescky R, Kraka E, Cremer D (2014) Inorg Chem 53:478–495
146. Gillespie A, Pittard K, Cundari T, White D (2002) Internet Electron J Mol Des 1:242–251
147. Cooney KD, Cundari TR, Hoffman NW, Pittard KA, Temple MD, Zhao Y (2003) J Am Chem Soc 125(14):4318–4324
148. Zeinalipour-Yazdi CD, Cooksy AL, Efstathiou AM (2008) Surf Sci 602(10):1858–1862
149. Fey N, Orpen AG, Harvey JN (2009) Coord Chem Rev 253(5-6):704–722
150. Fey N (2010) Dalton Trans 39:296–310
151. Frenking G, Fröhlich N (2000) Chem Rev 100:717–774
152. Thammavongsy Z, Kha IM, Ziller JW, Yang JY (2016) Dalton Trans 45(24):9853–9859
153. Mejuto C, Royo B, Guisado-Barrios G, Peris E (2015) Beilstein J Org Chem 11:2584–2590
154. Wünsche MA, Mehlmann P, Witteler T, Buß F, Rathmann P, Dielmann F (2015) Angew Chem Int Ed Engl 54(40):11857–11860
155. Geeson MB, Jupp AR, McGrady JE, Goicoechea JM (2014) ChemComm 50:12281–12284
156. Tobisu M, Morioka T, Ohtsuki A, Chatani N (2015) Chem Sci 6:430–437
157. Marín M, Moreno JJ, Navarro-Gilabert C, Álvarez E, Maya C, Peloso R, Nicasio MC, Carmona E (2018) Chem Eur J 25(1):260–272

158. Couzijn EPA, Lai YY, Limacher A, Chen P (2017) Organometallics 36:3205–3214
159. Yong X, Thurston R, Ho CY (2019) Synthesis 51:2058–2080
160. Francos J, Elorriaga D, Crochet P, Cadierno V (2019) Coord Chem Rev 387:199–234
161. Xu T, Sha F, Alper H (2016) J Am Chem Soc 138:66629–66635
162. Kim B, Park N, Lee SM, Kim HJ, Son SU (2015) Polym Chem 6:7363–7367
163. Mata JA, Hahn FE, Peris E (2014) Chem Sci 5:1723–1732
164. Makedonas C, Mitsopoulou CA (2007) Eur J Inorg Chem 2007(26):4176–4189
165. Crabtree R (2006) J Organomet Chem 691:3146–3150
166. Kégl TR, Pálinkás N, Kollár L, Kégl T (2018) Molecules 23:3176–3187
167. Zhang X, Yan X, Zhang B, Wang R, Guo S, Peng S (2018) Transit Met Chem 44:39–48
168. Mehlmann P, Dielmann F (2019) Chem Eur J 25(9):2352–2357
169. Romeo R, Alibrandi G (1997) Inorg Chem 36(21):4822–4830
170. Denny JA, Darensbourg MY (2016) Coord Chem Rev 324:82–89
171. Bungu PN, Otto S (2011) Dalton Trans 40(36):9238–9249
172. Ai P, Danopoulos AA, Braunstein P (2016) Dalton Trans 45(11):4771–4779
173. Xamonaki N, Asimakopoulos A, Balafas A, Dasenaki M, Choinopoulos I, Coco S, Simandiras E, Koinis S (2016) Inorg Chem 55:4771–4781
174. Oliveira KC, Carvalhoa SN, Duartea MF, Gusevskaya EV, dos Santos EN, Karroumi JE, Gouygou M, Urrutigoity M (2015) Appl Catal A Gen 497:10–16
175. Marín M, Moreno JJ, Alcaide MM, Álvarez E, López-Serrano J, Campos J, Nicasio MC, Carmona E (2019) J Organomet Chem 896:120–128
176. Valdes H, Poyatos M, Peris E (2015) Inorg Chem 54(7):3654–3659
177. van Weerdenburg BJ, Eshuis N, Tessari M, Rutjes FP, Feiters MC (2015) Dalton Trans 44 (35):15387–15390
178. Tapu D, McCarty Z, Hutchinson L, Ghattas C, Chowdhury M, Salerno J, VanDerveer D (2014) J Organomet Chem 749:134–141
179. Maser L, Schneider C, Vondung L, Alig L, Langer R (2019) J Am Chem Soc 141:7596–7604
180. Xu X, Zhang Z, Huang S, Cao L, Liu W, Yan X (2019) Dalton Trans 48:6931–6941
181. Yasue R, Yoshida K (2019) Organometallics 38(9):2211–2217
182. Czerwinska I, Far J, Kune C, Larriba-Andaluz C, Delaude L, De Pauw E (2016) Dalton Trans 45(15):6361–6370
183. Weinberger DS, Lavallo V (2015) Ruthenium olefin metathesis catalysts supported by cyclic alkyl aminocarbenes (CAACs). In: Grubbs RH, Wenzel AG, O'Leary DJ, Khosravi E (eds) Handbook of metathesis: catalyst development and mechanism. Wiley-VCH Verlag GmbH, Berlin, pp 87–95
184. Borguet Y, Zaragoza G, Demonceau A, Delaude L (2015) Dalton Trans 44(21):9744–9755
185. Check CT, Jang KP, Schwamb CB, Wong AS, Wang MH, Scheidt KA (2015) Angew Chem Int Ed Engl 54(14):4264–4268
186. Gallien AKE, Schaniel D, Woiked T, Klüfers P (2014) Dalton Trans 43:13278–13292
187. Varnado Jr CD, Rosen EL, Collins MS, Lynch VM, Bielawski CW (2013) Dalton Trans 42 (36):13251–13264
188. Yazdani S, Silva BE, Cao TC, Rheingold AL, Grotjahn DB (2019) Polyhedron 161:63–70
189. Poë AJ, Moreno C (1999) Organometallics 18(26):5518–5530
190. Gaydon Q, Cassidy H, Kwon O, Lagueux-Tremblay PL, Bohle DS (2019) J Mol Struct 1192:252–257
191. Bhattacharya A, Naskar JP, Saha P, Ganguly R, Saha B, Choudhury ST, Chowdhury S (2016) Inorg Chim Acta 447:168–175
192. Schulze B, Schubert US (2014) Chem Soc Rev 43(8):2522–2571
193. Mampa RM, Fernandes MA, Carlton L (2014) Organometallics 33:3283–3299
194. Strohmeier W, Muller FJ (1967) Chem Ber 100:2812–2821
195. Portnyagin IA, Nechaev MS (2009) J Organomet Chem 694(19):3149–3153
196. Magee TA, Matthews CN, Wang TS, Wotiz J (1961) J Am Chem Soc 83:3200–3203
197. Bond AM, Carr SW, Colton R (1984) Organometallics 3:541–548

198. Grim S, Wheatland D, McFarlane W (1967) J Am Chem Soc 89:5573–5577
199. Carlton L, Emdin A, Lemmerer A, Fernandes MA (2008) Magn Reson Chem 46(S1):S56–S62
200. Lang H, Meichel E, Stein T, Weber C, Kralik J, Rheinwald G, Pritzkow H (2002) J Organomet Chem 664(1-2):150–160
201. Möhring PC, Vlachakis N, Grimmer NE, Coville NJ (1994) J Organomet Chem 483 (1-2):159–166
202. Metters OJ, Forrest SJK, Sparkes HA, Manners I, Wass DF (2016) J Am Chem Soc 138 (6):1994–2003
203. Starosta R, Komarnicka UK, Puchalska M (2014) J Lumin 145:430–437
204. Andrella NO, Xu N, Gabidullin BM, Ehm C, Baker RT (2019) J Am Chem Soc 141 (29):11506–11521
205. Ciancaleoni G, Scafuri N, Bistoni G, Macchioni A, Tarantelli F, Zuccaccia D, Belpassi L (2014) Inorg Chem 53(18):9907–9916
206. Ciancaleoni G, Biasiolo L, Bistoni G, Macchioni A, Tarantelli F, Zuccaccia D, Belpassi L (2015) Chem Eur J 21(6):2467–2473
207. Collado A, Patrick SR, Gasperini D, Meiries S, Nolan SP (2015) Beilstein J Org Chem 11 (1):1809–1814
208. Rigo M, Habraken ERM, Bhattacharyya K, Weber M, Ehlers AW, Mézailles N, Slootweg JC, Müller C (2019) Chem Eur J 25:1–12
209. Lever A (1990) Inorg Chem 29:1271–1285
210. Lever A (1991) Inorg Chem 30:1980–1985
211. Suresh C, Koga N (2002) Inorg Chem 41:1573–1578
212. Giering W, Prock A, Fernandez A (2003) Inorg Chem 42:8033–8037
213. Alyea E, Song S (1996) Inorg Chem Comm 18:189–221
214. Coll DS, Vidal AB, Rodríguez JA, Ocando-Mavárez E, Añez R, Sierraalta A (2015) Inorg Chim Acta 436:163–168
215. Shi Q, Thatcher RJ, Slattery J, Sauari PS, Whitwood AC, McGowan PC, Douthwaite RE (2009) Chem Eur J 15:11346–11360
216. Valyaev DA, Brousses R, Lugan N, Fernandez I, Sierra MA (2011) Chem Eur J 17:6602–6605
217. Uppal BS, Booth RK, Ali N, Lockwood C, Rice CR, Elliott PIP (2011) Dalton Trans 40:7610–7616
218. Nelson DJ, Collado A, Manzini S, Meiries S, Slawin AM, Cordes DB, Nolan SP (2014) Organometallics 33(8):2048–2058
219. Donald KJ, Tawfik M, Buncher B (2015) J Phys Chem A 119(16):3780–3788
220. Verlinden K, Buhl H, Frank W, Ganter C (2015) Eur J Inorg Chem 2015(14):2416–2425
221. Flanigan DM, Romanov-Michailidis F, White NA, Rovis T (2015) Chem Rev 115:9307–9387
222. Kalescky R, Zou W, Kraka E, Cremer D (2014) Aust J Chem 67:426
223. Baker J, Pulay P (2006) J Am Chem Soc 128:11324–11325
224. Konkoli Z, Cremer D (1998) Int J Quantum Chem 67:1–9
225. Kraka E (2019) Int J Quantum Chem 119:e25849
226. Zou W, Kalescky R, Kraka E, Cremer D (2012) J Mol Model:1–13
227. Kalescky R, Zou W, Kraka E, Cremer D (2012) Chem Phys Lett 554:243–247
228. Kalescky R, Kraka E, Cremer D (2013) Mol Phys 111:1497–1510
229. Zou W, Cremer D (2016) Chem Eur J 22:4087–4097
230. McKean DC (1978) Chem Soc Rev 7:399–422
231. Hayward RJ, Henry BR (1975) J Mol Spectrosc 57:221–235
232. Kjaergaard HG, Yu H, Schattka BJ, Henry BR, Tarr AW (1990) J Chem Phys 93:6239–6248
233. Henry BR (1987) Acc Chem Res 20:429–435
234. Kjaergaard HG, Turnbull DM, Henry BR (1993) J Chem Phys 99:9438–9452
235. Rong Z, Henry BR, Robinson TW, Kjaergaard HG (2005) J Phys Chem A 109:1033–1041
236. Jacob CR, Luber S, Reiher M (2009) Chem Eur J 15:13491–13508
237. Jacob CR, Reiher M (2009) J Chem Phys 130:084106
238. Liegeois V, Jacob CR, Champagne B, Reiher M (2010) J Phys Chem A 114:7198–7212

239. Sokolov VI, Grudzev NB, Farina IA (2003) Phys Solid State 45:1638–1643
240. Sangster MJL, Harding JH (1986) J Phys C Solid State Phys 19:6153–6158
241. Woodward LA (1972) Introduction to the theory of molecular vibrations and vibrational spectroscopy. Oxford University Press, Oxford
242. Califano S (1976) Vibrational states. Wiley, London
243. Zou W, Tao Y, Freindorf M, Cremer D, Kraka E (2020) Chem Phys Lett 478:137337
244. Zou W, Cremer D (2014) Theor Chem Acc 133:1451
245. Kraka E, Larsson JA, Cremer D (2010) Generalization of the badger rule based on the use of adiabatic vibrational modes. In: Grunenberg J (ed) Computational spectroscopy. Wiley, New York, pp 105–149
246. Kalescky R, Kraka E, Cremer D (2013) J Phys Chem A 117:8981–8995
247. Kraka E, Setiawan D, Cremer D (2015) J Comput Chem 37:130–142
248. Sethio D, Daku LML, Hagemann H, Kraka E (2019) ChemPhysChem 20:1967–1977
249. Oliveira V, Kraka E, Cremer D (2016) Phys Chem Chem Phys 18:33031–33046
250. Oliveira V, Cremer D (2017) Chem Phys Lett 681:56–63
251. Yannacone S, Oliveira V, Verma N, Kraka E (2019) Inorganics 7:47
252. Oliveira VP, Marcial BL, Machado FBC, Kraka E (2020) Materials 13:55
253. Oliveira V, Cremer D, Kraka E (2017) J Phys Chem A 121:6845–6862
254. Oliveira V, Kraka E (2017) J Phys Chem A 121:9544–9556
255. Setiawan D, Kraka E, Cremer D (2015) J Phys Chem A 119:9541–9556
256. Setiawan D, Kraka E, Cremer D (2014) J Phys Chem A 119:1642–1656
257. Setiawan D, Kraka E, Cremer D (2014) Chem Phys Lett 614:136–142
258. Setiawan D, Cremer D (2016) Chem Phys Lett 662:182–187
259. Freindorf M, Kraka E, Cremer D (2012) Int J Quantum Chem 112:3174–3187
260. Tao Y, Zou W, Jia J, Li W, Cremer D (2017) J Chem Theory Comput 13:55–76
261. Tao Y, Zou W, Kraka E (2017) Chem Phys Lett 685:251–258
262. Makoś MZ, Freindorf M, Sethio D, Kraka E (2019) Theor Chem Acc 138:76
263. Lyu S, Beiranvand N, Freindorf M, Kraka E (2019) J Phys Chem A 123:7087–7103
264. Zhang X, Dai H, Yan H, Zou W, Cremer D (2016) J Am Chem Soc 138:4334–4337
265. Zou W, Zhang X, Dai H, Yan H, Cremer D, Kraka E (2018) J Organomet Chem 856:114–127
266. Tao Y, Zou W, Sethio D, Verma N, Qiu Y, Tian C, Cremer D, Kraka E (2019) J Chem Theory Comput 15:1761–1776
267. Tao Y, Qiu Y, Zou W, Nanayakkara S, Yannacone S, Kraka E (2020) Molecules 25:1589
268. Mpemba EB, Osborne DG (1969) Phys Educ 4:17–175
269. Kraka E, Cremer D (1990) Chemical implication of local features of the electron density distribution. In: Maksic ZB (ed) Theoretical models of chemical bonding. The concept of the chemical bond, vol 2. Springer, Heidelberg, p 453
270. Kraka E, Cremer D (1992) J Mol Struct Theochem 255:189–206
271. Setiawan D, Kraka E, Cremer D (2016) J Org Chem 81:9669–9686
272. Li Y, Oliveira V, Tang C, Cremer D, Liu C, Ma J (2017) Inorg Chem 56:5793–5803
273. Clar E (1972) The aromatic sextet. Wiley, New York
274. Setiawan D, Kalescky R, Kraka E, Cremer D (2016) Inorg Chem 55:2332–2344
275. Zhao Y, Truhlar DG (2008) Theor Chem Acc 120:215–241
276. Kendall RA, Dunning TH, Harrison RJ (1992) J Chem Phys 96(9):6796–6806
277. Picque N, Hänsch TW (2019) Nat Photonics 13:146–157
278. McIntosh AI, Yang B, Goldup SM, Watkinson M, Donnan RS (2012) Chem Soc Rev 41:2072–2082
279. Mantsch HH, Naumann D (2010) J Mol Struct 964:1–4
280. Parrott EPJ, Sun Y, Pickwell-MacPherson E (2011) J Mol Struct 1006:66–76
281. Smith E, Dent G (2019) Modern Raman spectroscopy: a practical approach. Wiley, New York
282. Smith DR, Field JJ, Wilson JW, Kane D, Bartels RA (2019) High-sensitivity coherent Raman spectroscopy with Doppler Raman. In: Conference on lasers and electro-optics. Optical Society of America, New York

283. Meier RJ (2007) Vib Spectrosc 43:26–37
284. Parks HL, McGaughey AJH, Viswanathan V (2019) J Phys Chem C 123:4072–4084
285. Yang Y, Schneider PE, Culpitt T, Pavosevic F, Hammes-Schiffer S (2019) J Phys Chem Lett 10:1167–1172
286. Humason A, Zou W, Cremer D (2014) J Phys Chem A 119:1666–1682
287. Badger RM (1934) J Chem Phys 2:128–131
288. Wiberg K (1968) Tetrahedron 24:1083–1096
289. Mayer I (2007) J Comput Chem 28:204–221
290. Porterfield WW (1993) Inorganic chemistry, a unified approach. Academic Press, San Diego
291. Anderson S (2004) Introduction to inorganic chemistry. University Science Books, Sausalito
292. Runyon JW, Steinhof O, Dias HVR, Calabrese JC, Marshall WJ, Arduengo AJ (2011) Austr J Chem 64:91165–91172
293. Arduengo AJ, Dolphin JS, Gurau G, Marshall WJ, Nelson JC, Petrov VA, Runyon JW (2013) Angew Chem Int Ed Engl 52:5110–5114
294. Nelson DJ, Nolan SP (2013) Chem Soc Rev 42:6723–6753
295. Hopkinson MN, Richter C, Schedler M, Glorius F (2014) Nature 510:485–496
296. Dröge T, Glorius F (2010) Angew Chem Int Ed Engl 49:6940–6952
297. Nelson DJ (2015) Eur J Inorg Chem 2015(12):2012–2027
298. Valdes H, Poyatos M, Peris E (2015) Organometallics 34:1725–1729
299. Jonek M, Diekmann J, Ganter C (2015) Chem Eur J 21:15759–15768
300. Fürstner A, Alcarazo M, Krause H, Lehmann CW (2007) J Am Chem Soc 129:12676–12677
301. Majhi PK, Serin SC, Schnakenburg G, Gates DP, Streubel R (2014) Eur J Inorg Chem 2014 (29):4975–4983
302. Soleilhavoup M, Bertrand G (2014) Acc Chem Res 48(2):256–266
303. Uzelac M, Hernán-Gómez A, Armstrong DR, Kennedy AR, Hevia E (2015) Chem Sci 6 (10):5719–5728
304. Becke AD (1988) Phys Rev A 38:3098–3100
305. Perdew JP (1986) Phys Rev B 33:8822–8824
306. Dunning TH (1989) J Chem Phys 90(2):1007–1023
307. Körsgen H, Urban W, Brown JM (1999) J Chem Phys 110(8):3861–3869
308. Carroll PK, McCormack P (1972) Astrophys J 177:L33–L36
309. DeYonker NJ, Allen WD (2012) J Chem Phys 137(23):234303
310. Nakazawa H, Itazaki M (2011) Fe-H complexes in catalysis. In: Plietker B (ed) Iron catalysis: fundamentals and applications. Springer, Berlin, pp 27–81
311. Aoto YA, de Lima Batista AP, Köhn A, de Oliveira-Filho AGS (2017) J Chem Theory Comput 13(11):5291–5316
312. Jones NO, Beltran MR, Khanna SN, Baruah T, Pederson MR (2004) Phys Rev B 70 (16):165406
313. Li HW, Zhu M, Buckley C, Jensen T (2018) Inorganics 6(3):91–96
314. Becke AD (1993) J Chem Phys 98(7):5648–5652
315. Hay PJ, Wadt WR (1985) J Chem Phys 82(1):299–310
316. Hay PJ, Wadt WR (1985) J Chem Phys 82(1):270–283
317. Wadt WR, Hay PJ (1985) J Chem Phys 82(1):284–298